Toward unbiased flow measurements in LHC proton-proton collisions

Master's thesis, 9.9.2024

Author:

Teemu Kallio

Supervisor:

Dong Jo Kim

UNIVERSITY OF JYVÄSKYLÄ
DEPARTMENT OF PHYSICS

Abstract

Teemu Kallio
Master's thesis
Toward unbiased flow measurements in LHC proton-proton collisions
Jyväskylä: University of Jyväskylä, 2024

Two-particle angular correlations of charged-particle pairs are studied in pp collisions at $\sqrt{s} = 13$ TeV with four different Monte-Carlo event generators. Correlation functions are constructed with relative azimuthal angle $\Delta\varphi$ and relative pseudorapidity distance $\Delta\eta$ between hadrons such as π, K, p and Λ particle pairs in multiple $\Delta\eta$ intervals. Using the low-multiplicity template fit method, enhanced jet yields in high-multiplicity events with respect to low-multiplicity events are subtracted. Due to a kinematic bias from jets and the difference in how event generators implement jet and flow components, subtraction of non-flow bias results in small systems. With a multiphase transport (AMPT) string melting model mass ordering of the extracted flow coefficients at low-p_T and particle type grouping at high-p_T ranges was observed. However, these characteristics are found to be different from results observed in large systems.

– **Keywords:** Event generator, low-multiplicity template fit method, flow measurement, ALICE, LHC

Tiivistelmä

Teemu Kallio
Pro-Gradu -tutkielma
Kohti tarkempia flow-mittauksia LHC:n protoni-protoni törmäytyksissä
Jyväskylä: University of Jyväskylä, 2024

Varattujen hiukkasparien kaksihiukkaskulmakorrelaatioita tutkittiin protoni-protoni törmäytyksissä $\sqrt{s} = 13$ TeV energioilla neljällä eri Monte-Carlo tapahtumageneraattorilla. Korrelaatiofunktiot muodostettiin useille $\Delta\eta$ väleille käyttäen suhteellista atsimuuttikulmaa $\Delta\varphi$ sekä suhteellista pseudorapiditeetti etäisyyttä $\Delta\eta$ hadron parien, kuten π, K, p ja Λ kesken. Suuren multiplisiteetin eventtien korostuneet jettisuihkut suhteessa pienen multiplisiteetin eventteihin poistettiin käyttäen pienen-multiplisiteetin mallin sovitus -menetelmää. Johtuen jettien tuottamasta kinemaattisesta vääristymästä sekä tapahtumageneraattoreiden tavasta toteuttaa jetti- ja flow-komponentteja, flow'hun liittymättömien komponenttien poistaminen vääristää tuloksia pienten systeemien tapauksissa. Säiesulauttamista (eng. String melting) implementoivalla monivaihekuljetusmallilla (eng. lyh. AMPT) havaittiin massajärjestäytymistä löydetyissä flow-kertoimissa pienillä poikittaisliikemäärillä sekä hiukkastyyppien ryhmäytymistä suurilla poikittaisliikemäärillä. Nämä löydökset poikkeavat suurten systeemien kanssa tehdyistä havainnoista.

– **Avainsanat:** Tapahtumageneraattori, pienen-multiplisiteetin mallin sovitus -menetelmä, flow-mittaus, ALICE, LHC

Acknowledgement

I would like to show my deepest gratitude to Dong Jo Kim who was my supervisor and provided guidance, encouragement as well as patience throughout the duration of this project. I am also grateful to Maxim Virta, Anna Önnerstad and to Cindy Mordasini from Jyväskylä ALICE group for helping me understand flow, research and things related. First and foremost, in the end, I would not be in this position without my family, friends and my beloved companion, who all kept me going through this journey.

Jyväskylä, 12.1.2024
Teemu Kallio

Personal contribution

As my personal contributions to the research I wrote an algorithm for the analysis method we used (low-multiplicity template fit method) and another algorithm for generating 2D scatter plots with data from same and mixed events. Another task for a further state in the research I modified plotting algorithms for identified particles and co-wrote one macro used for generating 2D arrays for plotting centrality and transverse-momentum dependent flow results. Furthermore I modified and improved visually the figures used in the paper. On writing the research paper, my role were about writing and refining the supplementary section which extended the details on two-particle correlation functions and the low-multiplicity template fit method. I also wrote references to the supplementary section from the main text and generated feedback for improvements in the main text. All programming work in the research was done using ROOT/C++ and Python programming languages.

Jyväskylä, 12.1.2024
Teemu Kallio

Contents

Chapter 1

Introduction

1.1 Ultra-relativistic heavy-ion collision

In the 1970's it was theorized that the very early universe was filled with extremely dense soup of quarks and gluons [1]. A quest to produce this state of matter, using high-energy collisions titled as "Little Bangs" in the spirit of cosmology, began in seventies. However, it took decades before announcing of first successful observations which came at the beginning of modern heavy ion collision era in 2000. That is when experiments with Relativistic Heavy Ion Collider (RHIC) first began by colliding Au-nuclei at $\sqrt{s_{NN}} =$ 130 GeV and $\sqrt{s_{NN}} = 200$ GeV center-of-mass energies [2]. These experiments found observables indicating of a transient intermediate state similar to the state right after the birth of the universe. Around ten years later, after releasing results from proton collisions in Compact-Muon-Solenoid (CMS) at the LHC (Large Hadron Collider) with $\sqrt{s_{NN}} = 7$ TeV collision energies, a new research area was discovered for lighter collision elements. These small system collisions, such as p+p, d+A and ^{3}He+A, showed many similar features found also with larger systems [3] [1].

In ultra-relativistic collisions events are generated with two atomic nuclei. At the collision the participating constituents inside these Lorentz-contracted particles interact predominantly through gluon fields as the protons and neutrons decoalesce into quarks. In this initial condition, the energy distribution is highly inhomogeneous on the transverse plane. Due to extremely high temperatures ($\sim 10^{12}$ K) and densities inside overlapping zone the particle mean free path is heavily reduced making the matter strongly coupled. At this pre-equilibrium stage medium starts to expand longitudinally and also radially in transverse plane to equilibrate itself. After extremely short time interval, around $\tau \approx 0.5 - 2.0$ fm/c, the medium is nearly equilibrated and describable with viscous hydrodynamics with deviations accounted as shear and bulk viscosity terms. At this stage interacting quarks and gluons exhibit collective motion and the medium is referred to as Quark-Gluon Plasma (QGP).

Subsequently the medium then cools off with expansion until it reaches crossover tem-

perature $T \approx 170$ MeV where quarks then coalesce to form hadrons again. In calculating this transition the hydrodynamic cells are boosted into lab frame producing momentum kick relative only to the mass of each hadron.
Phase following crossover transition consists of elastic and inelastic hadron scatterings until chemical freeze-out temperature is reached. Final interaction stage is described only by elastic collisions until temperature drops to kinetic freeze-out after which hadrons are free streaming until colliding with surrounding detector [4].

It is not possible to directly observe these intermediate stages, and thus experimental data is used in conjunction with simulation modelling in order to probe events (see Figure 1.1).

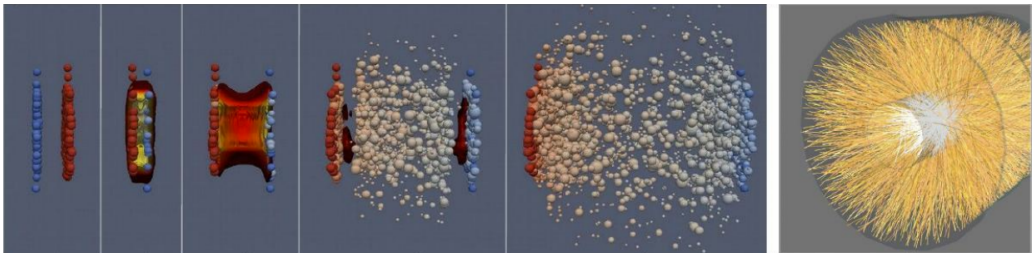

Figure 1.1: Visualization of a Pb–Pb collision at the LHC [5]. Initial collision is described in first picture from left showing two Lorentz contracted Pb-nuclei. Second image is a pre-equilibrium phase which has been modelled as particle free-streaming phase and also with hydrodynamics. Third image shows an equilibrium phase which is describing QGP formation. Fourth and fifth image describe hadronization stage where individual partons recombine into hadrons and interact with each other. Last picture is showing free streaming hadrons observed in the detector.

An important property of QGP is its shear viscosity to entropy ratio $\frac{\eta}{s}_{QGP}$ which value has been estimated to be roughly at $\frac{1}{4\pi}$ which is describing a medium as a nearly perfect fluid. This estimation (see Fig. 1.2) has been accomplished using calculations from string theory and also experimentally from experiments such as RHIC [6]. Ratio has been been extracted successfully also using machine learning algorithms with Bayesian analysis [7]. This method gives also constrains to correlated parameters producing information about the initial conditions of the collision.

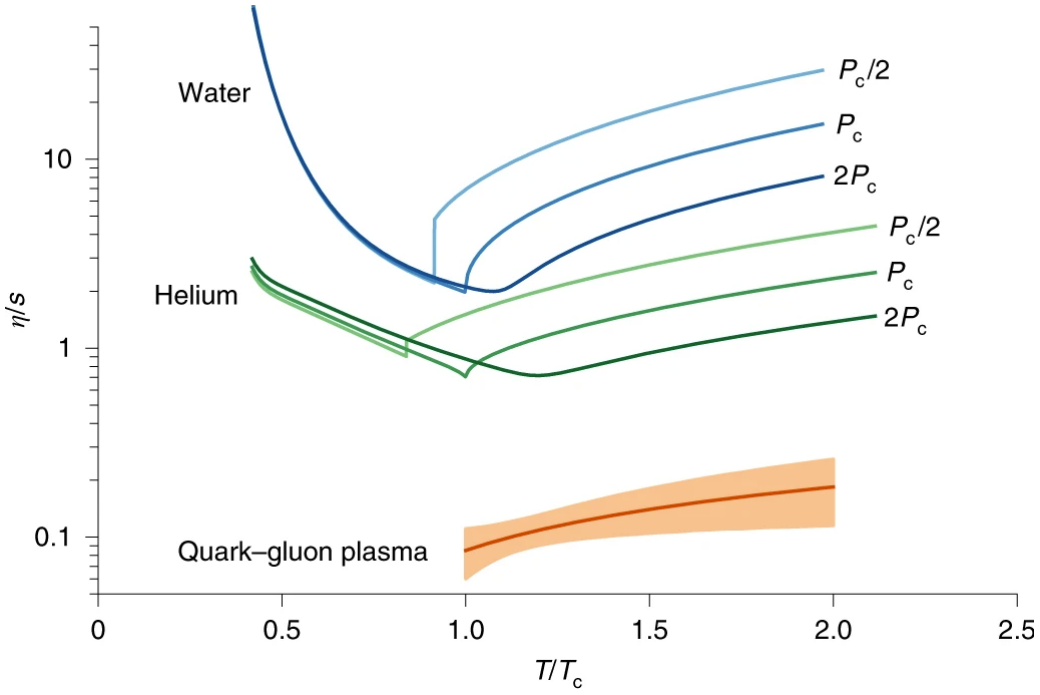

Figure 1.2: Common fluids in comparison to the estimated specific shear viscosity $\frac{\eta}{s}$(T) of QGP. Posterior median is shown in dark orange band and the 90% credible region for $\frac{\eta}{s}$ is indicated by orange area. This QGP estimation is calculated from Pb-Pb collision data at $\sqrt{s_{NN}}$ = 2.76 and 5.02 TeV. Shown comparable fluids are water (blue band) and helium (green band) and each band shows specific shear viscosity at different pressures relative to the critical pressure P_c [8].

It is thought that at the initial stages of QGP formation an irregular energy density distribution impacts the medium pressure-gradients that drive the expansion of the QGP droplet (see Figure. 1.4). This can be characterized by transforming from initial collision coordinate space to momentum space and using a Fourier series expansion to describe the final-state distribution of particles on transverse plane as function of azimuthal angle. The harmonic coefficients in this Fourier form representation are called harmonic flow observables.

From the early beginnings of modern heavy ion collision era experiments have shown a phenomenon called "double-ridge" and further studies have indicated its origins to lead to the initial collision geometry. This double-ridge refers to observable "bumps" when the yield of final-state particle distribution is organized using relative angular difference on the transverse plane and relative longitudinal distance between particle pairs (see Figure. 1.3). This structure was first thought to be observable only in large systems. However, similar double-ridge structure has recently been observed also in smaller collision systems rising the question if the phenomena are driven by same underlying mechanisms (see Fig. 1.5) [9, 10].

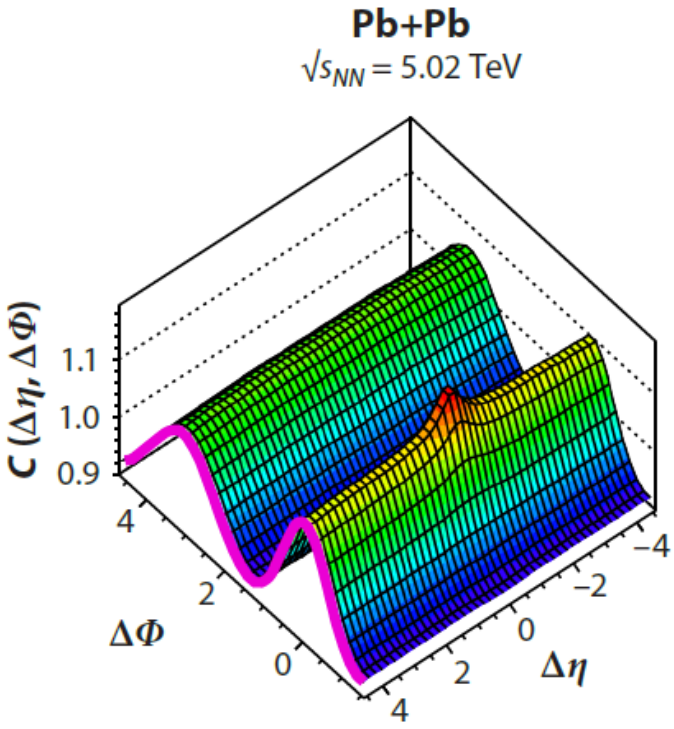

Figure 1.3: Two-particle correlation function of charged hadrons from high-multiplicity led-led collision event at the LHC. Figure shows a "double-ridge" structure seen as two distinct bumps at $\Delta\phi \approx 0$ and $\Delta\phi \approx \pi$. Relative angular distance of $\Delta\phi \approx 0$ is usually denoted as "near-side" where as $\Delta\phi \approx \pi$ is described as "away-side". Far-sides where relative distance $\Delta\eta$ is large are described as "long-range". Peak at $(\Delta\eta, \Delta\phi) = (0,0)$ originate from collimated particle showers called jets.

1.2 Small systems

Previously collisions such as d+Au, p+Pb and ^{3}He+Pb, referred as small systems, had been used only to control large system measurements as there was no expected flow in these events. In 2010 a double-ridge feature was observed at the CMS in proton-proton collision shown in Figure 1.5 [1]. After re-analysing of former small system experiments similar QGP signal was discovered also from these events.

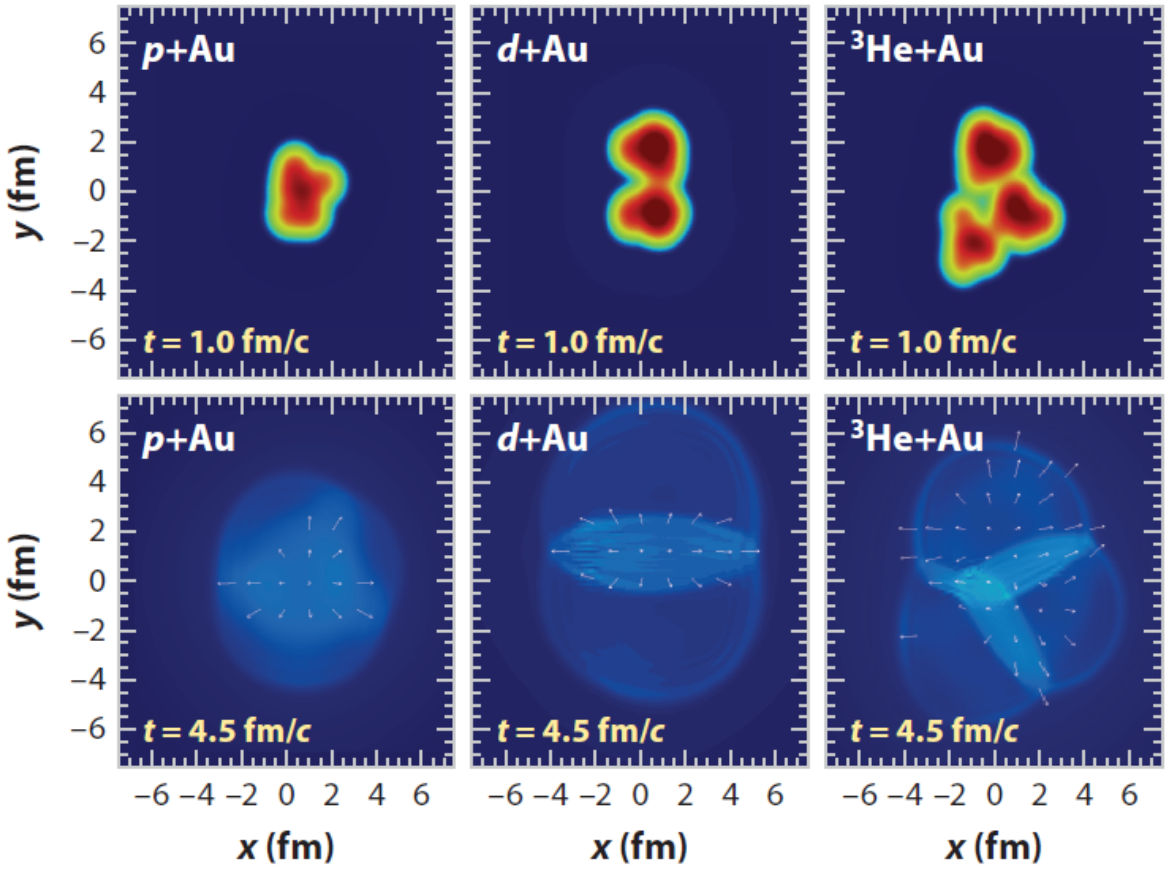

Figure 1.4: (upper row) Initial energy densities from p+Au, d+Au and ^{3}He+Au collision calculations from RHIC. Color scales correspond to local temperature. System size at t = 1.0 $\frac{\text{fm}}{\text{c}}$ varies approximately between 2 to 5 femtometers. Energy depositions called "hot spots" related to number of colliding constituents at initial collision are seen for each system making them predominantly circular, elliptical or triangular, respectively. (lower row) Results from utilizing Monte Carlo Glauber model to generate initial conditions showing pressure gradients as arrows. [4]

Sources other than QGP originated collective motion contribute also to the double-ridge structure. For example, in collision event a large amount of momentum can be transferred to a quark from the incoming particle via large momentum-transfer scattering. This can in effect produce two back-to-back collimated hadron showers called jet and di-jet. For larger A+A collisions these jets can be affected by the intermediate medium producing wider relative η-gap between particle pairs and thus contributing to away-side ($\Delta\phi \approx \pi$) and near-side ($\Delta\phi \approx 0$) yields in two-particle correlation function. Another source are decaying intermediate particles known as hadronic resonances which influence correlation function as contributions to near-side peak. These examples, also characterizing a phenomenon known as non-flow in hydrodynamic description, are largely complicating the flow measurements in small systems where collisions are dominated by

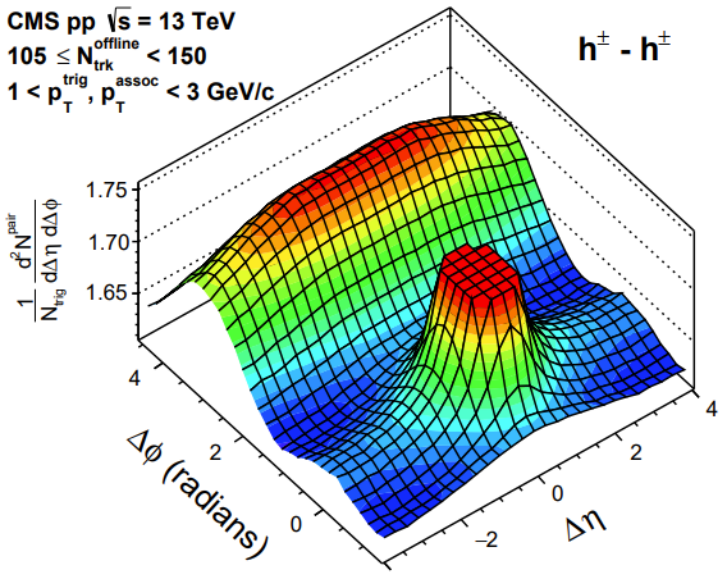

Figure 1.5: Two-particle correlation function from proton-proton collisions at the CMS in 2010. A double-ridge structure, similar as observed in large systems, is seen in the figure [11] as elongated low hillock at near-side. Large peak at $(\Delta\eta, \Delta\phi) = (0,0)$ originates from jets and is dominating the away-side yield over the extended ridge in $\Delta\eta$ entirely covering the away-side flow signal.

subevents.

There are multiple ways to test heavy ion standard model in case of small systems. One way is to measure correlation using multiple particles, a method known as multiparticle cumulant measurement. As QGP is characterized by flowing medium using multiparticle measurements the subgroup contributions are reduced resulting as flow amplitudes from collective motion. Other possibilities would be to manipulate initial conditions and test if the correlations scale with collision geometry or test if particle type flow produces patterns as particles in common velocity field are differentiated at hadronization by received momentum (see Figure. 1.6 for collision geometry scaling and evaluating simulation models).

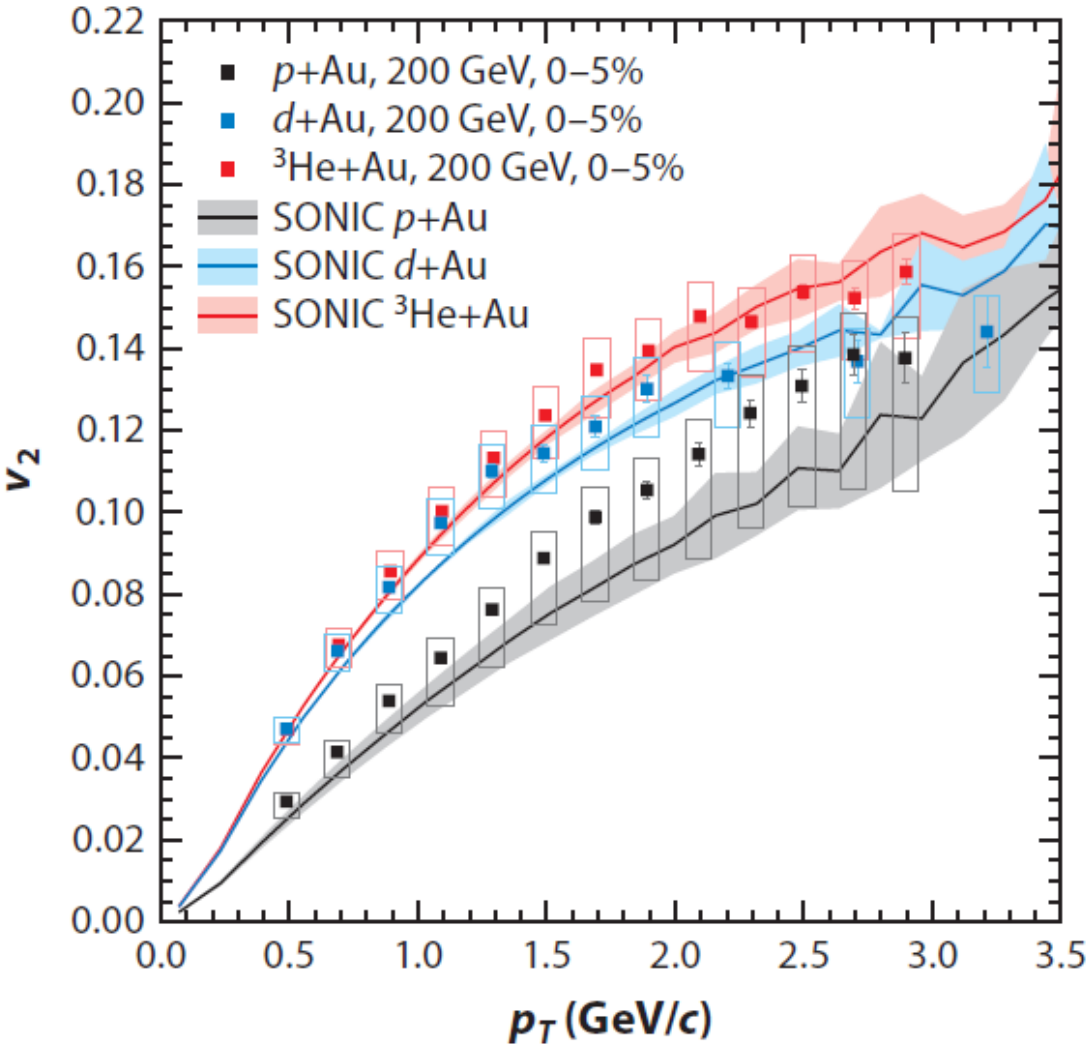

Figure 1.6: High-multiplicity v_2 for p+Au, d+Au and ^{3}He+Au for charged hadrons from hydrodynamic calculations (SONIC) and from experimental results (PHENIX) both with $\sqrt{s_{NN}}$ = 200 GeV collision energies. Figure shows that the hydrodynamic calculations are in good agreement with the experimental data. As SONIC incorporates Monte Carlo Glauber model (see Figure. 1.4) to generate the initial conditions, followed by later stage viscous hydrodynamics, the results suggest that initial geometry coupled with hydrodynamical evolution is valid framework for understanding the small system. [4]

However, as the non-flow in small collision systems is dominating events the aforementioned methods as such are not enough to extract reliably a small flow signal. For this a large number of alternative approaches, such as long-range correlations, have been developed in past few decades to subtract contaminating jets but these techniques have not solved the problem with large jet contamination at the away-side.

1.3 ALICE (A Large Ion Collider Experiment)

The ALICE experiment as part of the Large Hadron Collider (LHC) at CERN is dedicated to study the formation of QGP by colliding high energy particles such as Pb-nuclei. At the moment proton-proton collisions at ALICE detector occur at 13.6 TeV center-of-mass energies ($\sqrt{s}$ = 13 TeV) per particle pair. Collision remnants are collected by the surrounding detector parts and analyzed further by different ALICE Collaboration subgroups. Research on QGP can also provide insights into the very early universe and possibly to other extreme environments such as neutron star cores [12].

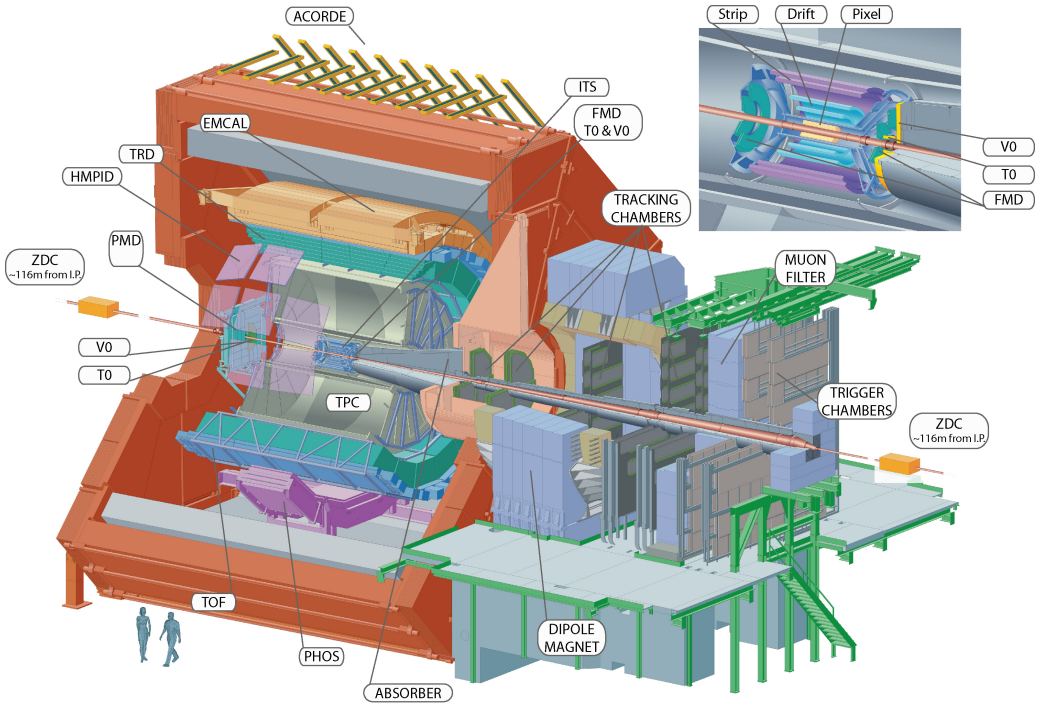

Figure 1.7: ALICE Experiment detector at LHC showing individual detector parts. (License: CC BY-SA 3.0)

ALICE Experiment uses a trigger system with selection methods for minimum bias (MB) events which can be constructed usually with "loose" triggers that accept a large fraction of the overall inelastic collision cross-section [13]. Detector also has about three millionths of a second (10^{-6} s) of time for responding and recording before the next collision occurs. For example, each collision can require a hit by two charged particles into two V-ZERO scintillator plates called V0A and V0C placed asymmetrically around interaction point. The actual data is then collected by different parts layered around the collision point located inside the Inner-Tracking-System (ITS) (see Fig. 1.7).

Chapter 2

Conceptual and mathematical frameworks

2.1 Collision planes and initial geometry

In the initial stage of the collision two planes can be constructed. There is a reaction plane Ψ_{RP} spanned by the detector beam line axis z and the perpendicular axis, the impact parameter b [4]. Another plane is the participant plane Ψ_{PP} which is spanned by the beam line axis z and by an axis related to spatial arrangement of the particles inside the overlapping zone, thus $\Psi_{RP} \neq \Psi_{PP}$. An event plane Ψ_{EP} refers to an angle from the reaction plane and as reaction plane is not accessible in the experiment, event planes are constructed from the final-stage observables.

A head-on collision produces roughly a circular shape while a non-central collision produces approximately an almond-shape overlapping zone on the plane perpendicular to beam direction called a transverse plane. The amount of overlapping in the collision between the particles is called as the centrality of the collision. Centrality is characterized by the impact parameter b, which is the distance between the two particle geometrical centers [14]. The average initial-state spatial eccentricity of a collision can be expressed as

$$\epsilon = \frac{\langle y^2 \rangle - \langle x^2 \rangle}{\langle y^2 \rangle + \langle x^2 \rangle} \tag{2.1}$$

where x and y are the transverse coordinates on transverse plane outlining the collision shape [15]. Eccentricity is related to the initial conditions of a collision. Particle location on transverse plane can be defined by azimuthal angle φ and by transverse momentum component p_T and is related to the final-state particle distribution.

2.2 Anisotropic flow

In a collision where QGP droplet is formed, the initial collision eccentricity leads to azimuthal anisotropy at the final-state distribution as function of azimuthal angle φ. This distribution can be expressed via a Fourier series representation as

$$\frac{dN}{d\varphi} \propto 1 + \sum_n 2v_n cos(n(\varphi - \Psi_n)) \tag{2.2}$$

where N is the amount of particles at angle φ, Ψ_n and φ are event plane and particle angles from the reaction plane. In Eq. 2.2 each term has a specific coefficient v_n related to the amplitude of the n'th harmonic.

Participant planes Ψ_{PP} are all related to the same per-event reaction plane Ψ_{RP} but these planes are not accessible to us. As an alternative way, from final-state description one can extract an event plane Ψ_{EP} which is related to the participant plane Ψ_{PP} and thus also to Ψ_{RP}. Partly due to fluctuating configurations of distributed partons and energy densities the initial state also fluctuates event-by-event. These fluctuations in turn affect following stages increasingly causing uncertainty in the averaged final-state observables and in the estimated event plane [16].

2.3 Event plane (EP) method

Reaction plane Ψ_{RP} can be approximated in numerical analysis (computational analysis). In order to get an approximation of the reaction plane one can calculate the mean particle direction calculating something called the Q-Vector per harmonic n over all of the final-state particle tracks in one event [17]

$$Q_n = \frac{\sum_{k=1}^{N} w_n^k u_n^k}{\sum_{k=1}^{N} w_n^k} = |Q_n| e^{in\Psi_n^{EP}} \tag{2.3}$$

where u_n^k is the k'th particle track unit-vector per harmonic n, N is the amount particles, w_n^k is the weight, commonly set as the particle p_T, for each track and Ψ_n^{EP} is the event plane azimuthal angle described as

$$-\frac{\pi}{n} < \Psi_n^{EP} < \frac{\pi}{n}. \tag{2.4}$$

showing that every increasing event plane resides in a smaller segment.

Essentially Q_n sums up each track to generate weighted average for direction of flow per harmonic n (flow expectation). There is also systematic error coming from the finite

detector resolution which needs to be corrected with

$$v_n = \frac{v_n^{obs}}{R_n} = \frac{\langle cos(n(\varphi - \Psi_n^{EP}))\rangle}{\langle cos(n(\Psi_n^{RP} - \Psi_n^{EP}))\rangle} \tag{2.5}$$

where v_n is the calculated flow amplitude, v_n^{obs} is the observed flow amplitude, R_n is the resolution factor to consider finite detector acceptance, φ is the particle angle relative to reaction plane Ψ^{RP} and Ψ^{EP} is the event plane angle also relative to reaction plane. Ψ_n^{RP} can be estimated using techniques such as approximating $\langle \Psi_n^{EP} \rangle$ using sub-events by dividing event transverse plane into n segments (see Eq. 2.4) where $n = 2, 3$ using Q-vector presentation for each sub-event.

Due to actual amount of particle tracks being always higher than what the detector is capable of detecting $\langle cos(n(\Psi_n^{RP} - \Psi_n^{EP}))\rangle < 1$ one of the systematic errors in extracting the anisotropic flow comes from the finite acceptance of the detector itself [18].

2.4 Extended two-particle angular correlations

Another way to calculate final-state correlation is to use relative angle between two particle tracks

$$\Delta\varphi = \varphi_i - \varphi_j \tag{2.6}$$

where i^{th} particle is usually called trigger particle and j^{th} particle is called trigger-associate particle. If this angle is taken from the final-state data, excluding double counting where $\Delta\varphi_{ij} = \Delta\varphi_{ji}$, the need to calculate event plane Ψ_n^{EP} is subtracted as the fluctuations average out by themselves

$$\langle cos(n(\varphi_i - \Psi_n - (\varphi_j - \Psi_n))\rangle \tag{2.7}$$

$$\langle cos(n(\varphi_i - \varphi_j + \Psi_n - \Psi_n))\rangle \tag{2.8}$$

$$\langle cos(n(\Delta\varphi_{ij})\rangle. \tag{2.9}$$

As each angle relates to a specific flow coefficient v_n this means that relating two particles per term we have flow amplitude coming from two particles and thus we have $v_{n,n}$ as the Fourier coefficients

$$\frac{dN^{pair}}{d\Delta\varphi} \propto 1 + \sum_n 2v_{n,n}cos(n\Delta\varphi) \tag{2.10}$$

which is a 1-dimensional distribution as a function of relative angle $\Delta\varphi$.

For a 2-dimensional discription of the position we need something called rapidity y which is defined as

$$y \equiv \frac{1}{2} ln(\frac{E - p_z c}{E + p_z c}) \tag{2.11}$$

where E is the energy of the particle and p_z is the momentum into the beam direction. Eq. 2.11 is useful in ultra-relativistic high energy collisions where particles move near at the speed of light and thus as you calculate particle state observable on the transverse plane, then p_z is zero and logarithm becomes 0. On the other hand if you have particle moving at c then the equation will go to $\pm\infty$. Still Eq. 2.11 becomes cumbersome to calculate due to the difficulty to measure energy and momentum of a high energy particle. For this we can derive from rapidity y more suitable form for ultra-relativistic situations. This is the pseudorapidity η of a particle and is defined only by the angle θ from the beam line z as

$$\eta \equiv -ln[tan(\frac{\theta}{2})]. \tag{2.12}$$

These relative azimuthal angles $\Delta\varphi$ and relative pseudorapidities $\Delta\eta$ between particles can then be described by the two-particle angular correlation function [19]

$$\frac{1}{N_{\text{trig}}} \frac{\mathrm{d}^2 N^{\text{pair}}}{\mathrm{d}\Delta\eta \mathrm{d}\Delta\varphi} = B_{max} \frac{S(\Delta\eta, \Delta\varphi)}{B(\Delta\eta, \Delta\varphi)} \Big| \tag{2.13}$$

where N_{trig} is the amount of trigger particles, N^{pair} is the amount of trigger and trigger-associate particle pairs, $S(\Delta\eta, \Delta\varphi)$ is the correlation function for particles from the same event, $B(\Delta\eta, \Delta\varphi)$ is the mixed distribution for trigger and associate particles from different events and B_{max} is the normalization value for mixed events.

Chapter 3

Flow extraction

3.1 Event generators

Simulation models, called event generators, implement heavy ion-collision physics to study and produce the experimental results. These implementations include thermal models modelling global thermal and chemical equilibrium, transport models only concentrating on non-equilibrium dynamics to models that only consider global equilibrium in the simulation [20]. Four different such Monte-Carlo event generators and a few million pp collision events per model was used in our research to study proton-proton collisions.

Models	Characteristics	Mechanism
PYTHIA8 default	Jets and no flow	
PYTHIA8 string shoving	Jets and flow	String repulsion
AMPT string melting	Jets and flow	String melting
EPOS4	Jets and hydro	Core (hydrodynamical)

Table 3.1: A list of the models with the main flow simulation mechanism.

In PYTHIA8 with default settings, model does not have partonic or hadronic interaction [21] to simulate flow and have thus been used for estimations for non-flow contributions. Other PYTHIA8 model with string shoving setting uses repulsive force between strings for microscopic transverse pressure producing long-range correlations. However, the way model simulates hard scatterings using strings have also been generating long-range correlation in low-multiplicity events [22] which is not in line with experimental data [23].

A multiphase transport model (AMPT) with a string melting setting simulates initial conditions, partonic scatterings, hadronization and hadronic scatterings and has been succesful in explaining hydrodynamical and non-hydrodynamical excitations in large and small systems [21].

EPOS4 can model full event evolution with its core and corona named processes. It simulates hydrodynamic expansion in its core process and hadronic interactions in the

corona [21]. These different generator models with their characteristic flow generation mechanisms, are listed in Table. 3.1.

3.2 Selecting events and particles

Same event selection constraints were applied to each model which meant using identical

Detector	Acceptance	Range
TPC	$\|\eta\| < 0.8$	$0.2 < p_{\mathrm{T}} < 6.0$ GeV/c
FMDA	$1.9 < \eta < 4.8$	$p_{\mathrm{T}} > 0.0$ GeV/c
FMDC	$-3.1 < \eta < -1.9$	$p_{\mathrm{T}} > 0.0$ GeV/c

Table 3.2: Detector acceptances with used p_T range

pseudorapidity η range as is the V0A ($2.8 < \eta < 5.1$) and V0C ($-3.7 < \eta < -1.7$) detector range of acceptance, with the p_T range specified for mid- and forward-rapidity as a condition when selecting individual charged particles from model event data (see Table. 3.2).

As the redistribution of energy into particle production and kinetic energy are highly related to the amount of charged-particles generated in the collision, multiplicity estimation is crucial part of the research [24]. Event multiplicity is estimated by calculating value for V0M which is the cumulative count of hits found in V0A and V0C detectors [21]. Then each event is divided with the mean multiplicity $\langle \mathrm{V0M} \rangle$ for normalized multiplicity distribution. This way multiplicities are categorized into percentiles for estimations of individual event multiplicities [25]. In this research $60-100\%$, $40-60\%$, $40-20\%$ and $20-0\%$ percentile bins was used to characterize events.

Multiplicity percentiles from different generators can be seen in Fig. 3.1. Vertical lines 0–5%, 5–20% and 60–100% indicate probabilities to generate an event with specific multiplicity [25] in AMPT string melting model. For example, 0–5% area indicates percentage of high-multiplicity ($+80$ N_{ch}) events out of all generated collisions. For each percentile different particles in transverse momentum range $0.2 < p_{\mathrm{T}} < 6$ GeV/c is identified using specific particle ID numbers (PID's) and identification functions provided by each event generator.

Final-state charge-particle yields as function of η seen in Fig. 3.2 show models following trend of the experimental data well at mid-rapidity while some differ in relative yields toward experiments from ALICE Collaboration. For PYTHIA8 default and EPOS4 these yields are bar with the experimental data. In contrast, PYTHIA8 string shoving shows large difference toward yields from ALICE while AMPT string melting exhibits smaller deviations from experiments [21]. Forward-rapidity trend could show difference between some of the models relative to experiments, which can be seen especially in EPOS4. Higher transverse momentum shows smaller yields, which is expected due to higher amount of particles reside at lower p_T ranges. However, this is not clear with AMPT string melting at $0.8 < p_T < 1.3$ GeV range, where there is visible saturation of final-state particles.

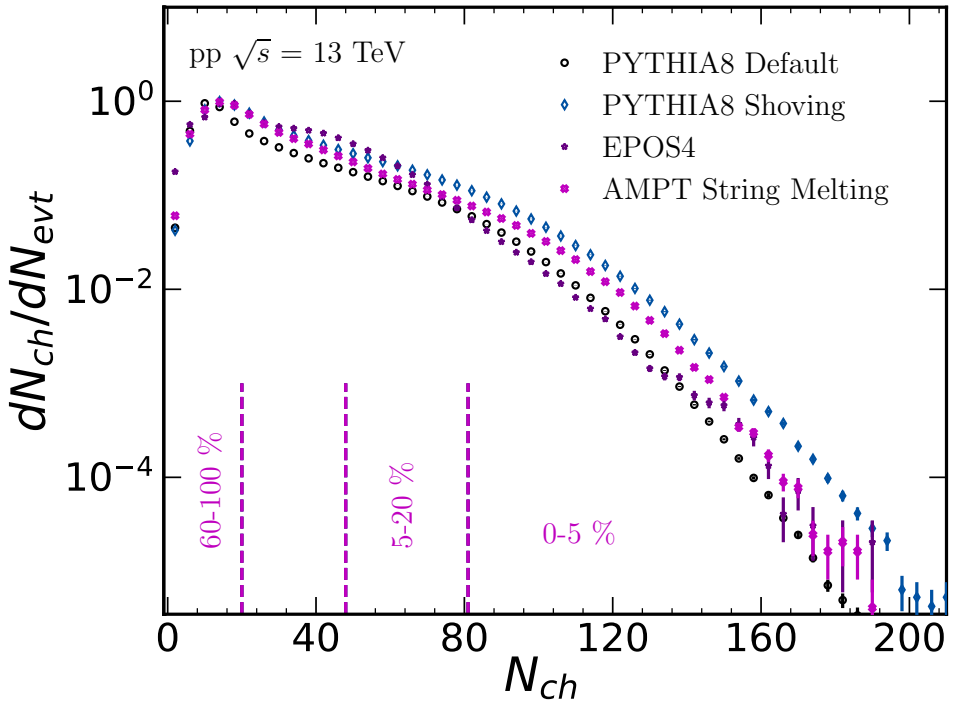

Figure 3.1: Charged-particle multiplicity estimations with ⟨V0M⟩ for all four models. Vertical bars indicating multiplicity classes for AMPT string melting model.

This could be partly due to radial flow pushing lower p_T particles to higher transverse momentum ranges.

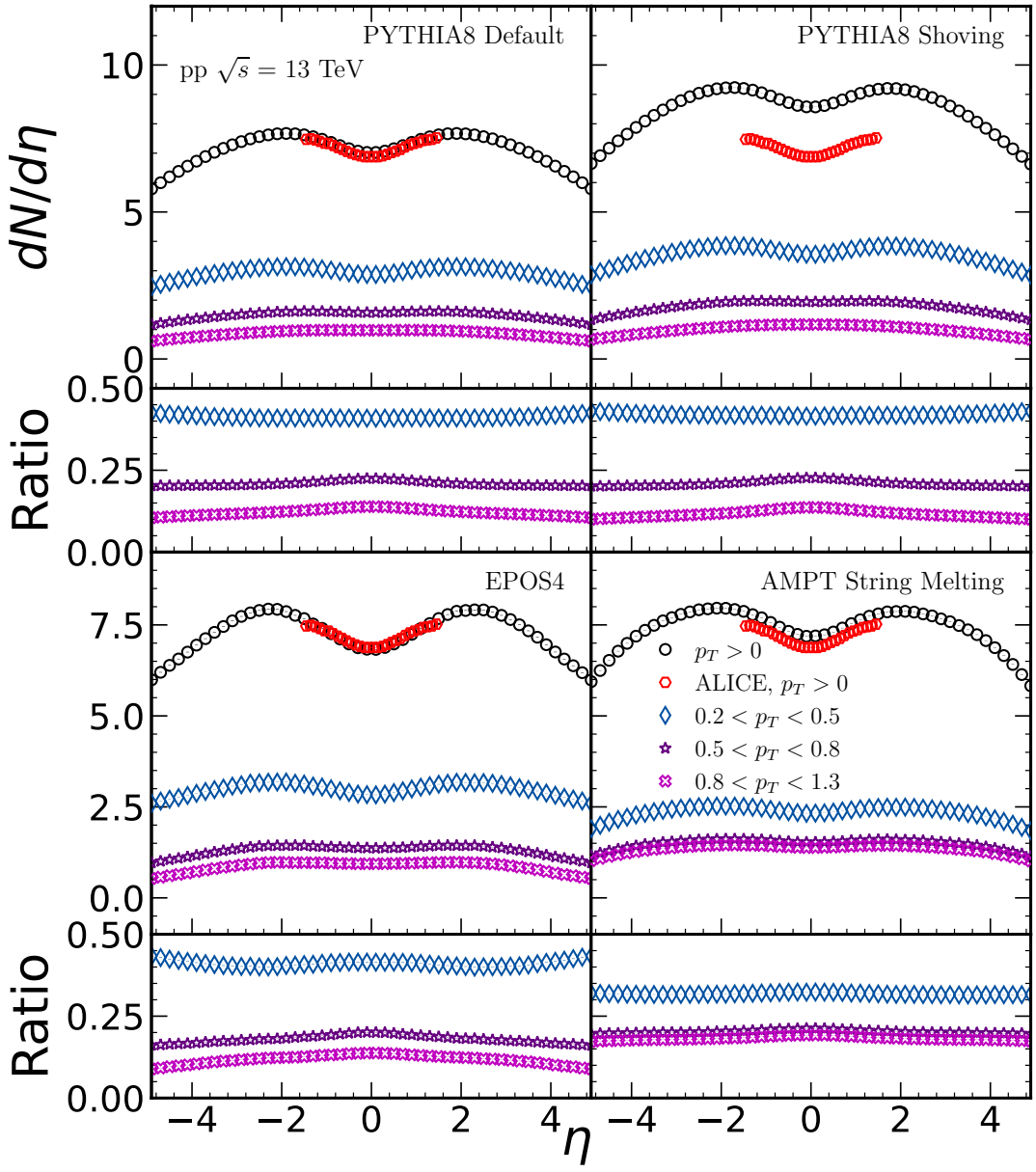

Figure 3.2: Charged-particle pseudorapidity density over large η range for different p_T intervals. Results are shown from all four models and are compared to mid-rapidity results from ALICE Collaboration.

3.3 Two-particle angular correlations

In this research, two-particle angular correlations (see Eq. 2.13) for each model was measured. Correlations were constructed by dividing same event distribution $S(\Delta\eta, \Delta\varphi)$ with normalized mixed event distribution $B(\Delta\eta, \Delta\varphi)/B_{max}$ where B_{max} was the mixed event maximum. This was done to each calculated multiplicity percentile per model [21].

Two-particle correlations from PYTHIA8 with default setting are shown in Fig. 3.3. As the main problem with extracting flow from small systems are dominating high-p_T particles seen as collimated particle showers, TPC-FMD correlations was used to increase pseudorapidity distance $\Delta\eta$ between particle pairs. In the results from TPC-FMDC a long elongated jet yield reaching up to $|\Delta\eta| \approx 4$ can be seen showing that the jet contributions reach up to exceptionally long-range correlations.

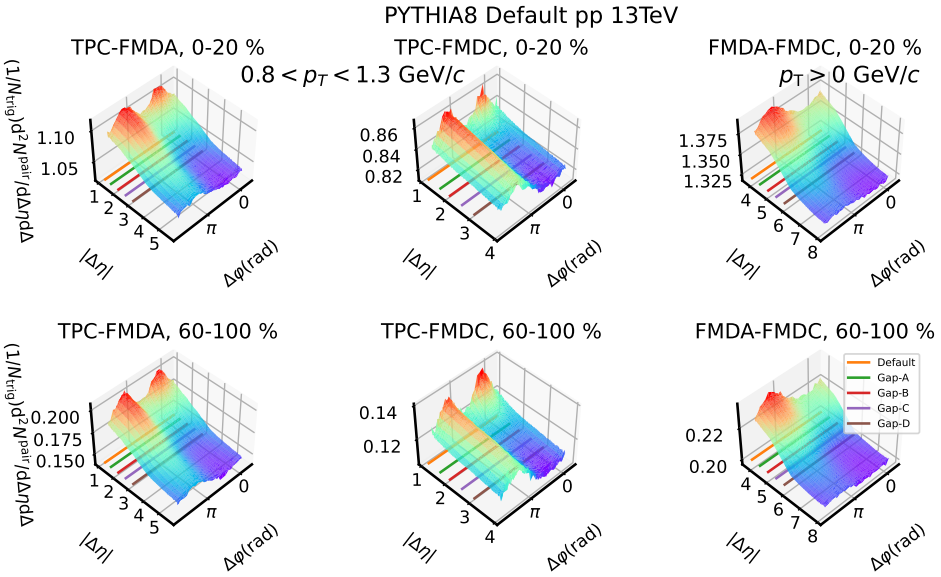

Figure 3.3: Two-particle correlation functions from PYTHIA8 default. Figures displaying three different particle acceptance combinations (TPC-FMDA, TPC-FMDC and FMDA-FMDC) for low- and high-multiplicity percentiles. Colored bars are indicating various $\Delta\eta$-gaps used in the analysis. TPC-FMDA and TPC-FMDC results are from intermediate p_T range where as FMDA-FMDC plots are from $p_{\mathrm{T}} > 0$ GeV/c.

Correlations	Default	Gap-A	Gap-B	Gap-C	Gap-D
TPC-FMDA	[1.1, 5.6]	[1.5, 5.6]	[2.0, 5.6]	[2.5, 5.6]	[3.0, 5.6]
TPC-FMDC	[1.1, 3.9]	[1.6, 3.9]	[2.0, 3.9]	[2.5, 3.9]	[3.0, 3.9]
FMDA-FMDC	[3.8, 7.9]	[4.3, 7.9]	[4.8, 7.9]	[5.3, 7.9]	[5.8, 7.9]

Table 3.3: $\Delta\eta$-gaps for each combination of detectors. TPC covering mid-rapidity and FMD-detectors covering forward-rapidity range.

Furthermore, these jets are seen decreasing in $|\Delta\eta|$ in Fig. 3.3 and also similar decrease is seen in Fig. 3.4 from AMPT string melting. The indicated color bars are $\Delta\eta$-gaps used in the analysis and described in Tab. 3.3.

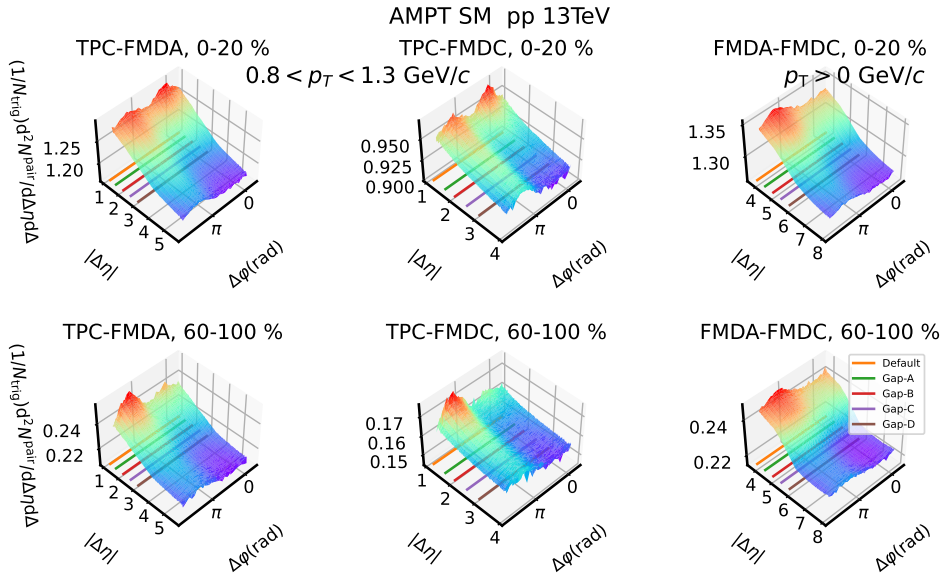

Figure 3.4: Two-particle correlation functions from AMPT string melting. Figures displaying three different particle acceptance combinations (TPC-FMDA, TPC-FMDC and FMDA-FMDC) for low- and high-multiplicity percentiles. Colored bars are indicating various $\Delta\eta$-gaps used in the analysis. TPC-FMDA and TPC-FMDC results are from intermediate p_T range where as FMDA-FMDC plots are from $p_{\mathrm{T}} > 0$ GeV/c.

3.4 Low-multiplicity template fit method

Due to large fragmentation of jets in small systems where there are less particles interacting causing the high-p_T particles to dominate events, and due to the di-jets coming from momentum conservation, the away-side ($\Delta\varphi \sim \pi$) is contaminated [26]. These circumstances make it difficult to extract flow even at long-range because away-side jet yield is significantly larger.

Nevertheless, as experiments such as ATLAS has observed (see Fig. 3.5) that for enough low multiplicities long-range correlation yield at near-side is shown to be zero.

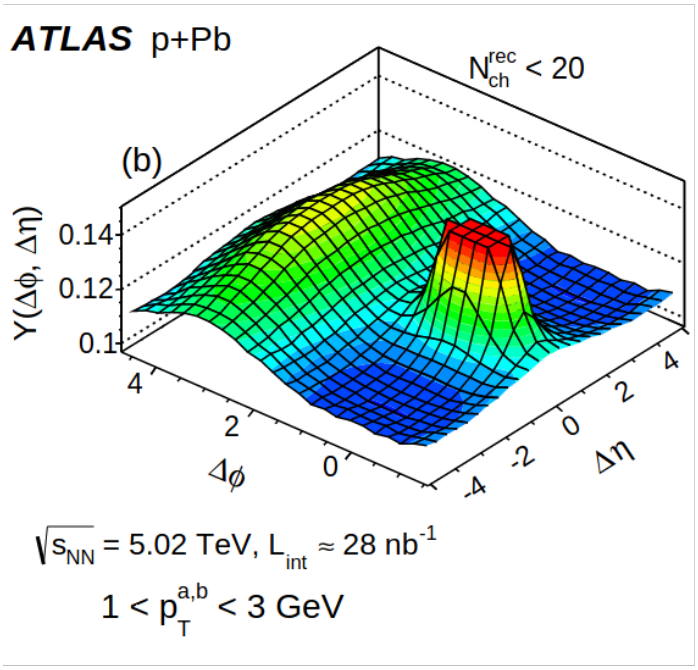

Figure 3.5: Long-range near-side per-trigger yield in p-Pb collision at intermediate p_T from ATLAS Collaboration showing flat near-side yield for $|\Delta\eta| > 2$ [27].

With the assumption that in these events there are jets only on the away-side and no near-side flow, a low-multiplicity yield can be used to subtract jets from high-multiplicity away-side yields. This includes a second assumption that the away-side yield shapes are independent of multiplicity. Jet yield subtraction can then be done with the following equation relating high-multiplicity $Y_{\mathrm{HM}}(\Delta\varphi)$ and low-multiplicity $Y_{\mathrm{LM}}(\Delta\varphi)$ yields [26]

$$\begin{aligned} Y_{\mathrm{HM}}(\Delta\varphi) = G\ (1 &+ 2v_{2,2}\cos(2\Delta\varphi) \\ &+ 2v_{3,3}\cos(3\Delta\varphi) \\ &+ 2v_{4,4}\cos(4\Delta\varphi) \\ &+ F\ Y_{\mathrm{LM}}(\Delta\varphi), \end{aligned} \tag{3.1}$$

where $Y_{\mathrm{HM}}(\Delta\varphi)$ contains both flow and jet components, G is a pedestal factor, Fourier terms are corresponding to different flow harmonics while term coefficients are the measured flow amplitudes $v_{n,n}$, $FY_{\mathrm{LM}}(\Delta\varphi)$ is the low-multiplicity yield without near-side structure multiplied by the relative difference between high-multiplicity and low-multiplicity (the 60–100% percentile) jet yields (see Fig. 3.6).

While these assumption are to a degree supported by experimental data [28], there are systematic uncertainties present when relative difference between extracted flow without away-side jet subtraction and flow obtained with LMTF method is large [26]. From ATLAS Collaboration results [26] can be seen that the template fit is also more sensitive to higher order flow fluctuations with increasing multiplicities.

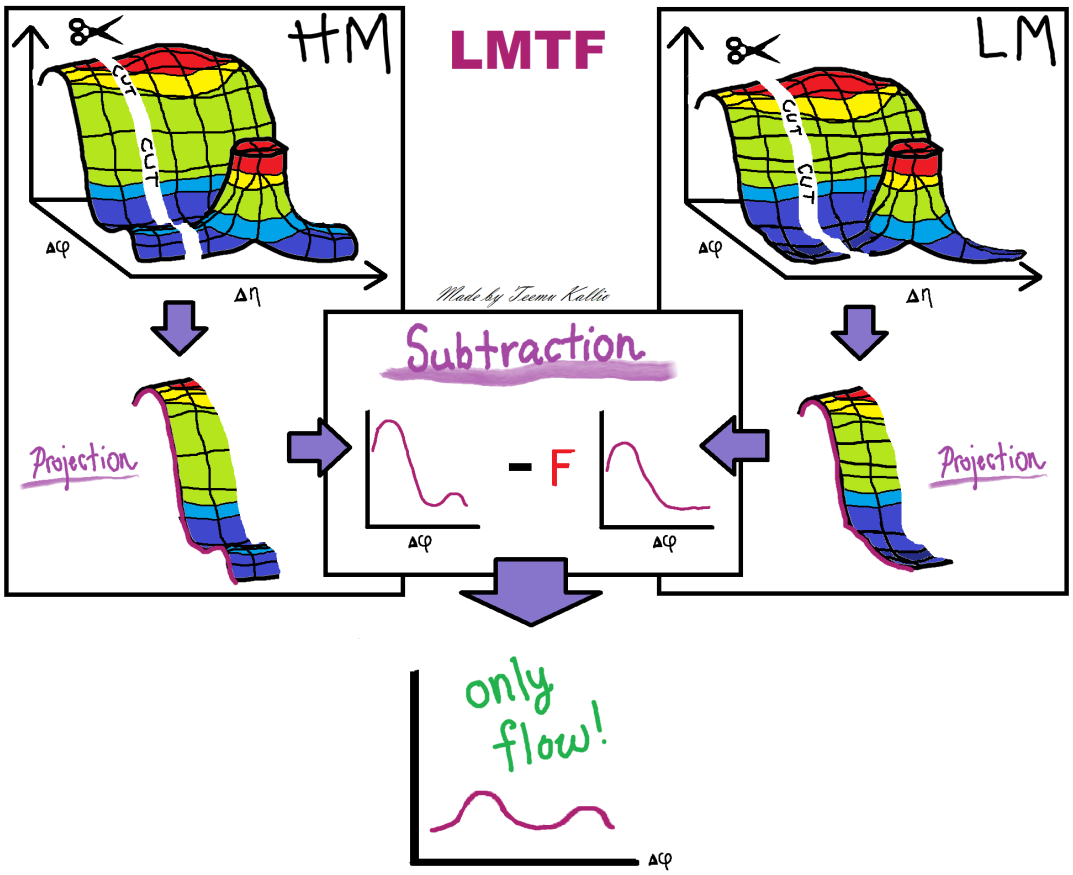

Figure 3.6: A schematic of the non-flow subtraction done to a two-particle correlation function in analysis with low-multiplicity template fit method (referred later as LMTF method).

As extracted flow amplitudes from LMTF method are two-particle coefficients a single particle coefficient needs to be calculated separately. This is done by assuming a medium with only flow. With this a product of two different particle flow coefficients can be generated

$$V_{n,\Delta}(p_T^a, p_T^b) = v_{p_T^a} v_{p_T^b} \tag{3.2}$$

and using a method proposed by PHENIX Collaboration flow coefficient v_n from three different groups of particles are calculated, consisting three different detector acceptances, with the following equation [29, 21]

$$v_n(p_{\mathrm{T,TPC}}) = \sqrt{\frac{v_{n,n}^{\mathrm{TPC-FMDA}} \cdot v_{n,n}^{\mathrm{TPC-FMDC}}}{v_{n,n}^{\mathrm{FMDA-FMDC}}}}. \tag{3.3}$$

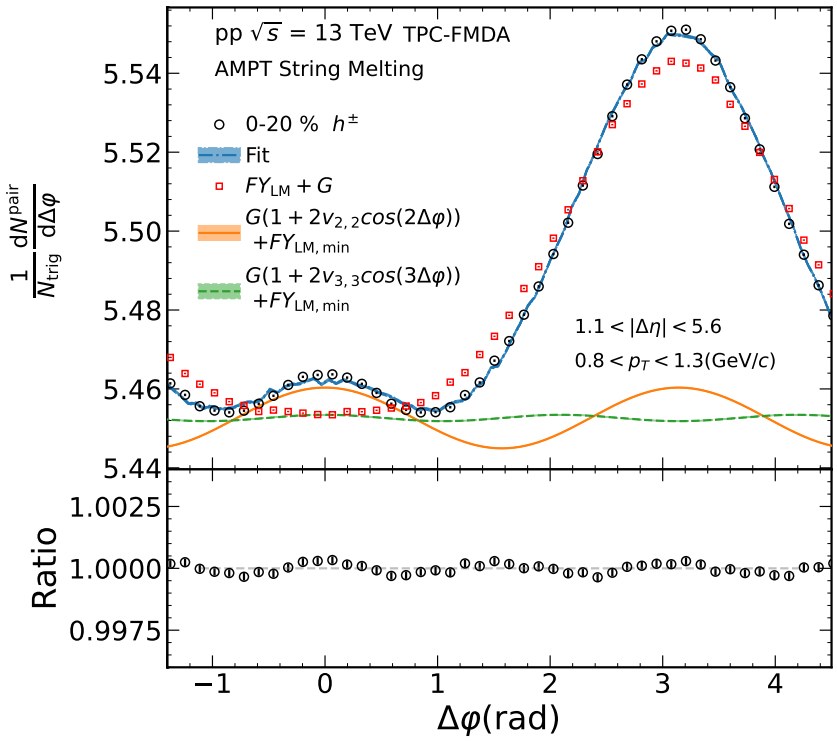

Figure 3.7: LMTF results from unidentified hadron data displaying 0-20% signal as black markers, fit as blue band and red squares as corresponding to the low-multiplicity template. Orange and green signals are the extracted v_2 and v_3 signals.

LMTF results from AMPT string melting is shown in Fig. 3.7 which is from the TPC-FMDA combination. Even with the default $\Delta\eta$-gap no ridge structure on the near side is seen in the band describing low-multiplicity yield, which indicates that there is almost no jet contamination. The figure also shows the $v_{2,2}$ and $v_{3,3}$ components, with $v_{2,2}$ being the dominant component. For this same reason, gap-D was used with other models as well to generate low-multiplicity correlation yield for the analysis and jet yield subtraction.

Using AMPT string melting model, which showed no near-side yield, jet shape modification ratio could be estimated for other models, shown in Fig. 3.8. PYTHIA8 default, PYTHIA8 string shoving and EPOS4 models was divided with results from AMPT string melting. For AMPT string melting and EPOS4 there is no ridge seen in the near-side. For away-side, AMPT string melting shows broader shape than EPOS4 when compared to results from PYTHIA8 models. These observed near-side yields from PYTHIA8 default and PYTHIA8 string shoving are not in line with the first assumption of LMTF method.

Next a collage of three per-trigger particle yields is seen in Fig. 3.10 after LMTF analysis where results are from TPC-FMDA combination over default $\Delta\eta$-gap. A per-trigger particle low-multiplicity yield ridge at near-side can be seen in every plot. Due to these observations also EPOS4 was shown not fill the first LMTF assumption.

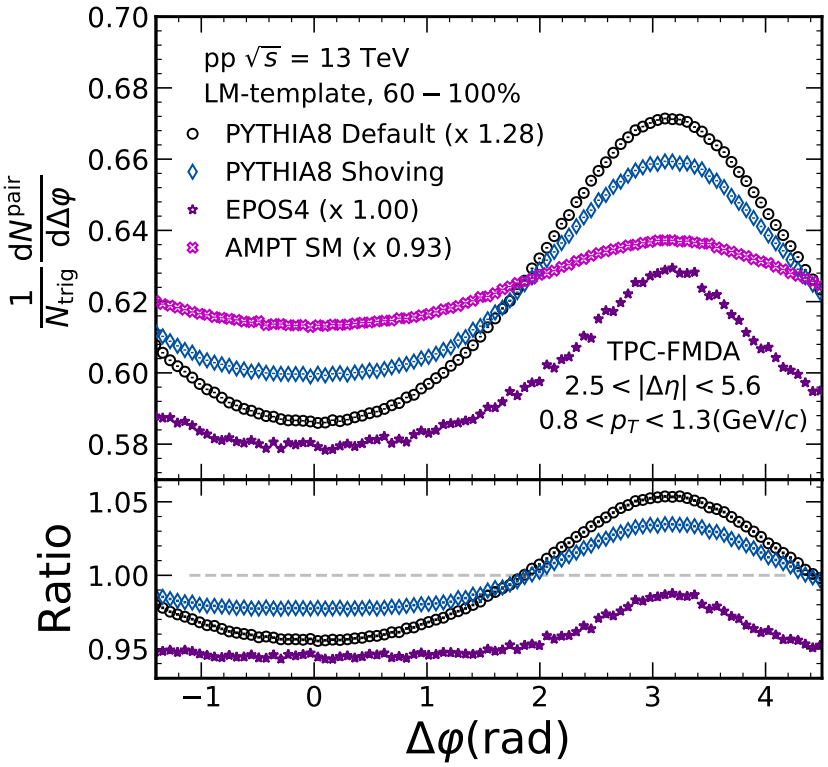

Figure 3.8: Low-multiplicity per-trigger particle yields at intermediate p_T range from TPC-FMDA for the different model calculations using the default gap. Yields are scaled to highlight more clearly the result shapes.

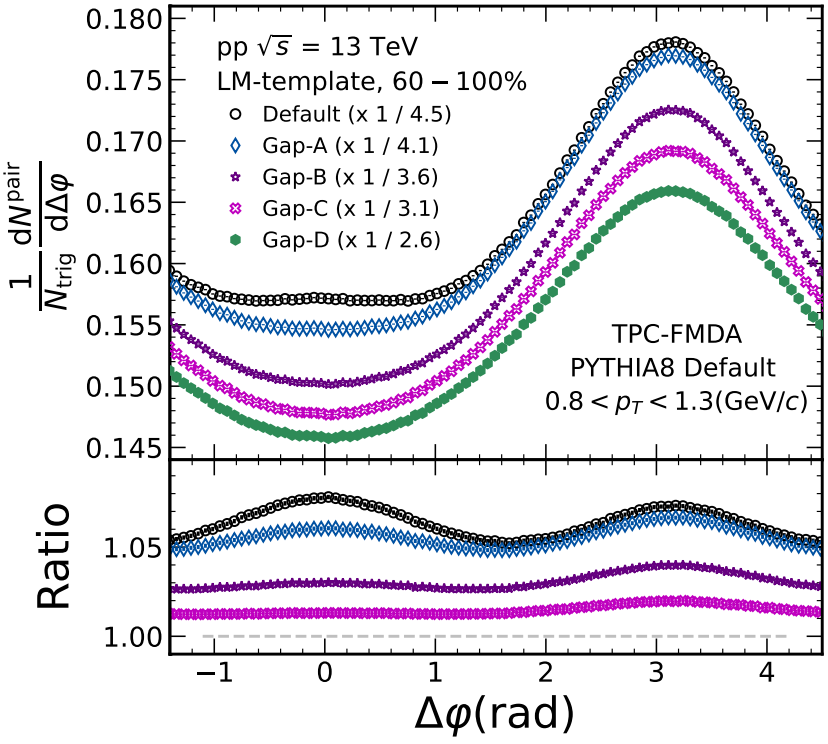

Figure 3.9: Low-multiplicity per-trigger particle yields from PYTHIA8 default showing decreasing yields as function of η-gap range scaled with $\frac{1}{\Delta(\Delta\eta)}$. Relative difference to gap-D is seen in the ratio plot.

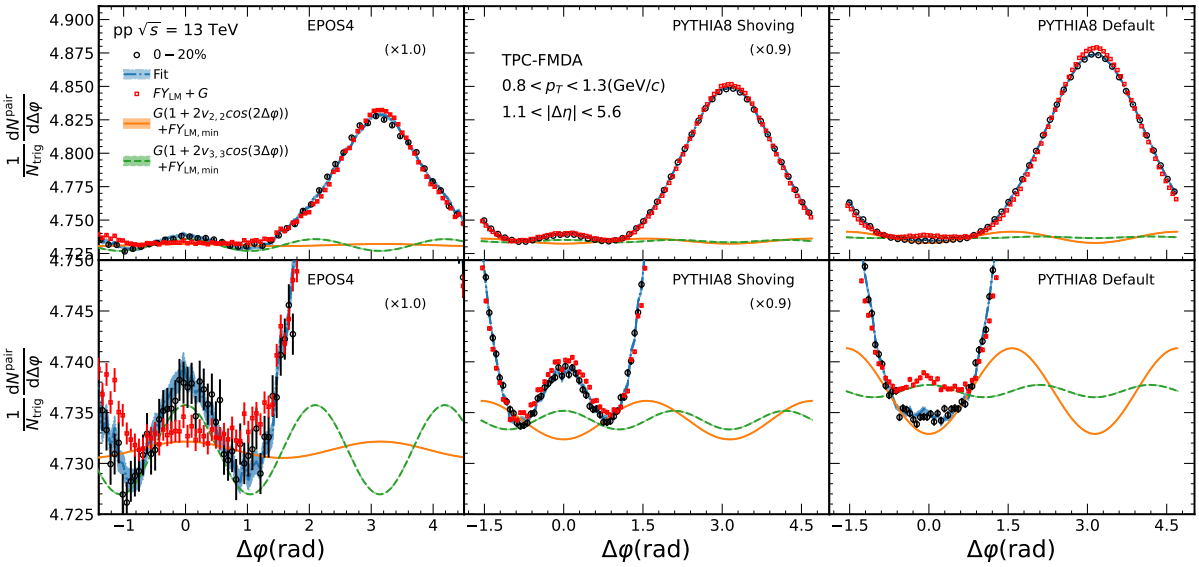

Figure 3.10: Figure of EPOS4, PYTHIA8 string shoving and PYTHIA8 default template fit results side-by-side. Black markers are showing $0-20\%$ multiplicity percentile signal. Red squares are corresponding to scaled low-multiplicity while orange and green functions are presenting the LMTF extracted v_2 and v_3 harmonic flow.

3.5 Computational analysis with LMTF method

Following section is for explaining how flow extraction was done to the constructed two-particle correlation functions (e.g. see Fig. 3.4 and Fig. 3.3). Data preparation and analysis were done using ROOT framework and figures in the paper were created with Python programming language along with its data visualization libraries (i.e. Matplotlib library).

Each step of analysis procedure is first explained in order and then represented as a stripped down version of the code so as to retain clarity in the Sec. A (Appendix).

Steps in the analysis:

1. Two-particle correlation functions are first constructed using same $S(\Delta\eta, \Delta\varphi)$ and mixed $B(\Delta\eta, \Delta\varphi)$ event scatter plots and B_{max} for normalization shown as snippet code in Listing A.1.

2. Then the two-particle functions are projected into $\Delta\varphi$ in Listing A.1.

3. After which 1D-projections are sent as two parameters $(Y(\Delta\varphi)_{LM/HM})$ to a macro for χ^2-testing from which most fitting parameters are extracted and saved which is shown as code in Listing A.3.

4. After chi-square testing for most fitting parameter values program goes into doing low-multiplicity template fitting on the data. Here the low-multiplicity histogram is multiplied by now minimized F value with added normalization factor G to get

$$Y_{HM,jet} = FY_{LM} + G \tag{3.4}$$

which describes the jet yields in the case of related high-multiplicity event without modulation from the flow component.
If now, using Eq. 3.4, jet contamination is subtracted from $\mathrm{Y_{HM}}$, with flow and jet components, a distribution with only flow components is generated. This flow be then extracted using the Fourier decomposition

$$G(1 + 2\Sigma_n[v_{n,n}cos(n\Delta\varphi)]) \tag{3.5}$$

as a fit function.

Then the minimum multiplicity bin $(60 - 100\%)$, corresponding to low-multiplicity histogram, is multiplied by F factor to scale the fit correctly to the signal. The fit is then saved and a text file is made to hold most fit parameters per specific data variants (multiplicity, pseudorapidity and p_T interval) including $v_{n,n}$ for second and third harmonic and their errors along with integers corresponding to the current selection of data variants. This part of the algorithm is shown partly in Listing. A.4.

5. Next TGraphError graph templates are generated from saved flow coefficients to plot flow results with Python data visualization tools seen in Listing. A.5 (plotting of figures with Python is not shown in code).

Chapter 4

Results

In Figure 4.1 is shown $v_{2,2}$ from two different detector combinations TPC-FMDA and TPC-FMDC along with the calculated v_2 which is a combination of resulted $v_{2,2}$ of charged hadrons. All measured flow components are shown for each separated $\Delta\eta$-gap and for all models.

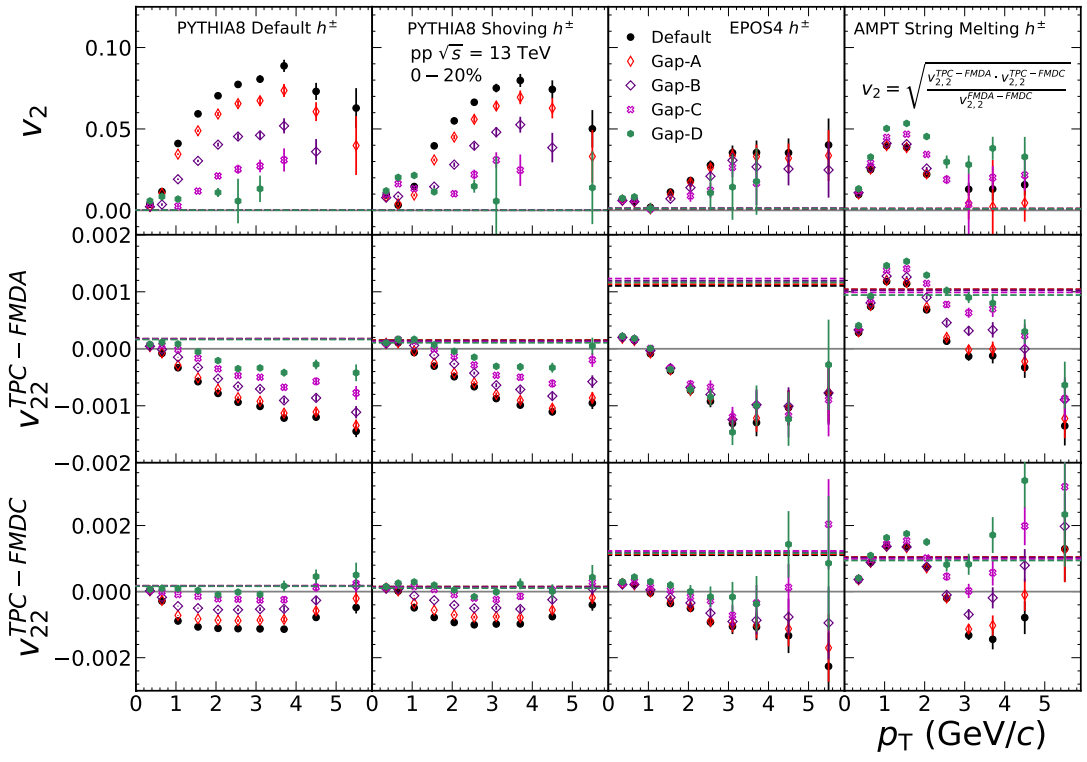

Figure 4.1: Calculated high-multiplicity v_2 along with $v_{2,2}$ results from TPC-FMD combinations for different $\Delta\eta$-gaps at $\sqrt{s} = 13$ TeV. Dashed lines in each panel are showing extracted $v_2^{FMDA-FMDC}$ and $v_{2,2}^{FMDA-FMDC}$ coefficients from each $\Delta\eta$ interval.

PYTHIA8 default shows unexpected non-zero flow over all $\Delta\eta$-gaps while PYTHIA8 string shoving displays similar lower v_2 yield. Decreased flow from string shoving can come from subtracting non-flow with low-multiplicity near-side yield (see Fig. 3.10) [21]. From EPOS4 flow yields are lower than with PYTHIA8 string shoving and the relation to $\Delta\eta$-gap is not as clearly seen. Nevertheless between all η-gap regions decreasing v_2 is seen. For AMPT string melting the results are showing different relation with saturated v_2 at lower transverse momentum regions and a decrease of v_2 after $p_T > 2$ GeV. For the most part this is due to jet contamination at lower $\Delta\eta$-gap regions resulting increased flow amplitudes with increasing η [21].

Since the gap-D has lowest non-flow yields results are shown only from this η region from AMPT string melting model.

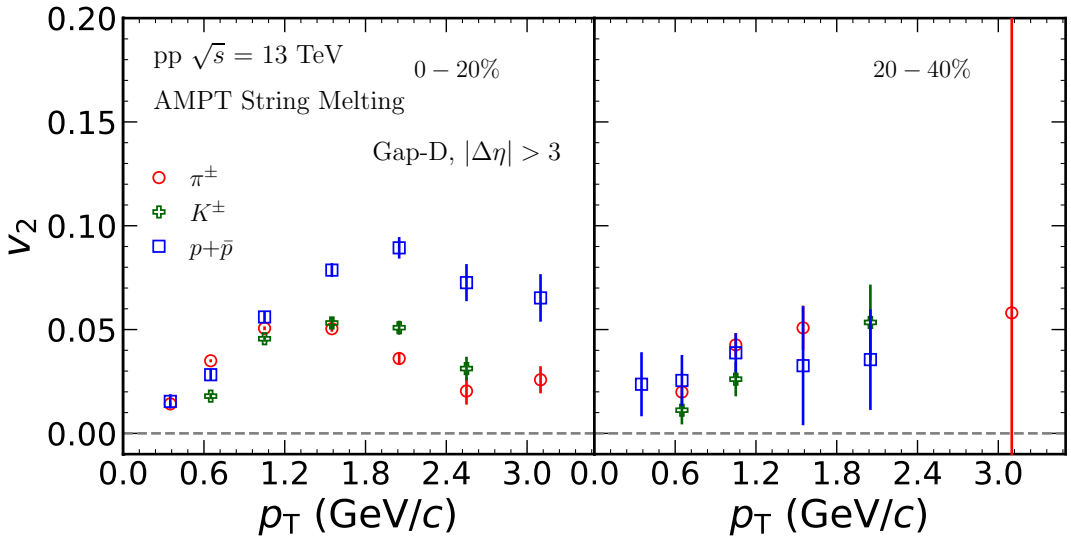

Figure 4.2: High-multiplicity v_2 results as function of transverse momentum from AMPT string melting model showing flow amplitudes for $\pi^{\pm}$, $K^{\pm}$, $p + \overline{p}$ particles.

Figure 4.2 displays calculated v_2 where particle type grouping becomes visible with high-p_T in 0–20% multiplicity percentiles. Even so grouping behaviour seem to disappear with lower multiplicities as seen in the panel for 20–40% multiplicity percentile. The difference between two multiplicities for grouping and splitting effects led us to study also the multiplicity dependence of v_2.

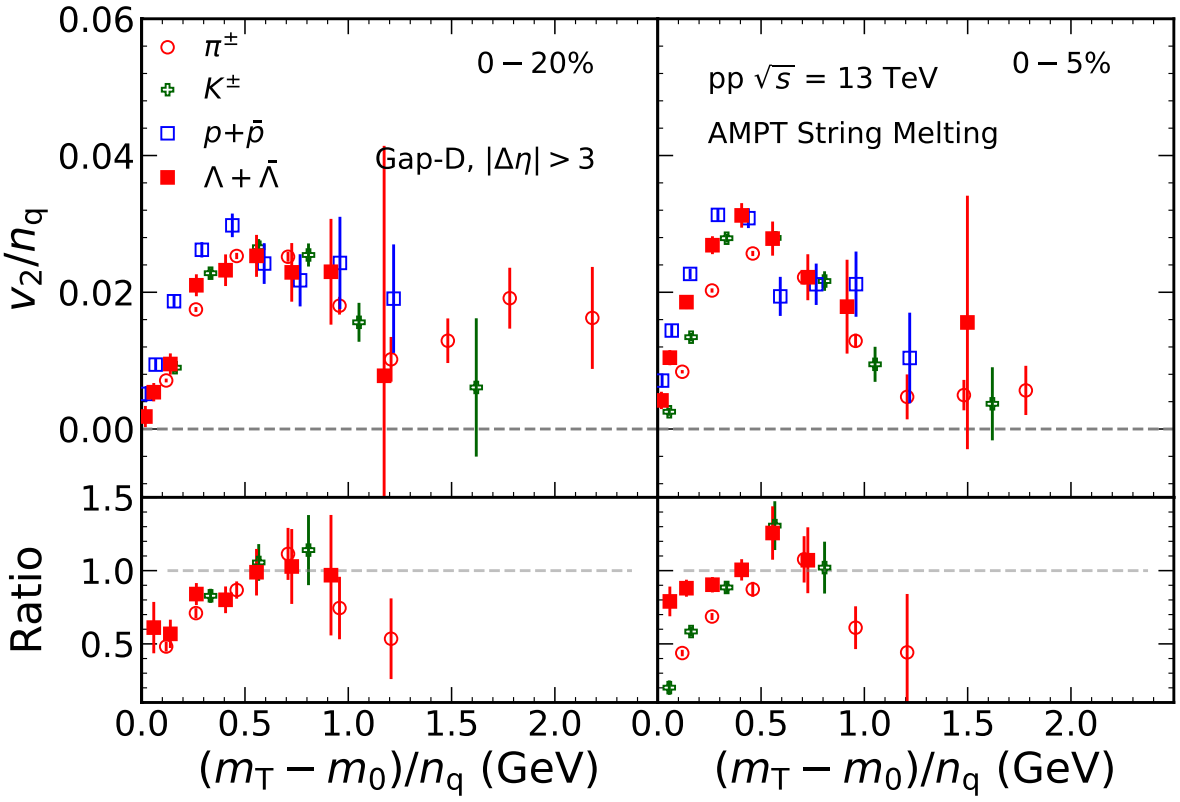

Figure 4.3: Quark-number scaled v_2 as function of transverse kinetic energy $\mathrm{KE_T}$ for multiple particle types from AMPT string melting model results.

The figure above (Fig. 4.3) exhibits transverse kinetic energy $\mathrm{KE_T}$ dependent v_2 that has been normalized by dividing elliptic flow coefficients with the number of quarks per particle. Shown results indicate that these grouping behaviours come from partonic interactions [21]. However, large system studies from RHIC and especially LHC show different and more concentrated quark-scaled v_2. In addition, PbPb-collisions with $\sqrt{S_{NN}} = 5.02$ TeV from ALICE show also particle type grouping across multiplicities at higher transverse kinetic energies even with quark-number scaling seen in Fig.4.4. A wider p_T range can provide more insight into NCQ-scaling in small systems [21].

Figure 4.5 shows v_2 as function of multiplicity in two p_{T} ranges for $|\Delta\eta| > 3$. The transverse momentum ranges shown are $0.8 < p_{\mathrm{T}} < 1.3, \mathrm{GeV}/c$ and $1.3 < p_{\mathrm{T}} < 1.8, \mathrm{GeV}/c$. Results show elliptical flow for $\mathrm{h}^{\pm}$, $\pi^{\pm}$, $\mathrm{K}^{\pm}$, $\mathrm{p} + \bar{\mathrm{p}}$ and $\Lambda + \bar{\Lambda}$ particle where particles are arranged approximately by their masses such that more massive particles generate more flow which increases also with multiplicity. Other experiments have shown decreasing v_2 toward lower multiplicities while what is seen from AMPT is showing linear decrease toward lower multiplicities and a change around when multiplicity count reach 50 for both p_T ranges. For $1.3 < p_{\mathrm{T}} < 1.8, \mathrm{GeV}/c$ range the separation for v_2 gets clearer and particle type grouping along with mass ordering is seen when particle count reaches over 50. For multiplicities lower than 50, results from AMPT show saturated v_2. Fig. 4.5 shows lighter

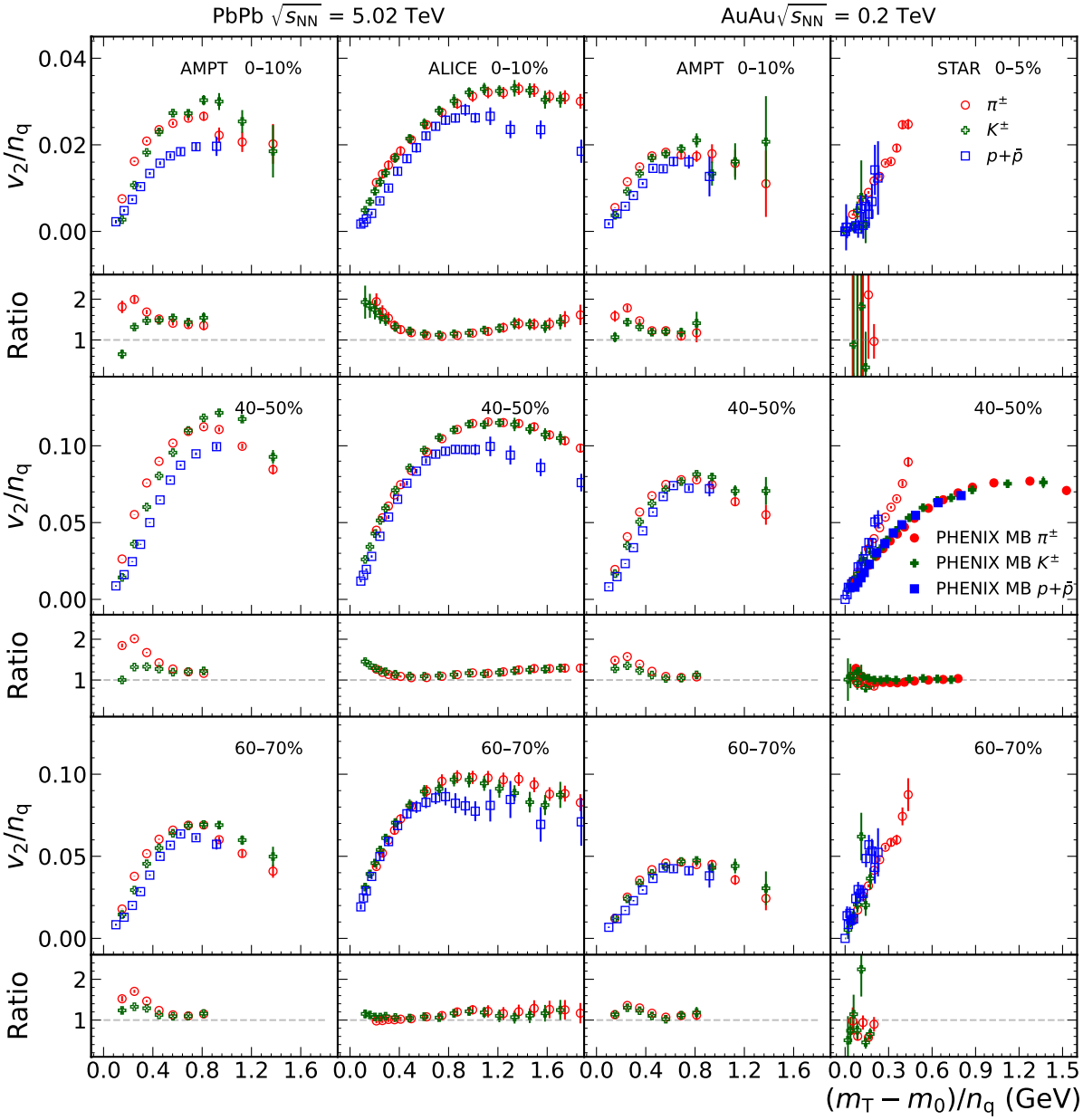

Figure 4.4: Quark-scaled v_2 as function of transverse kinetic energy from Pb-Pb and Au-Au studies. Each column shows multiplicity cut with three different percentiles ($0-10\%$, $40-50\%$, $60-70\%$) from AMPT model along with experimental results from ALICE (LHC) and STAR (RHIC) Collaborations. The PHENIX Collaboration (RHIC) results are shown only for the minimum bias Au-Au collisions.

mesons react more to the increased multiplicity at $p_T > 13$ GeV which can be observed by the decreased v_2 whereas heavier baryons gain more flow from the increased trans-

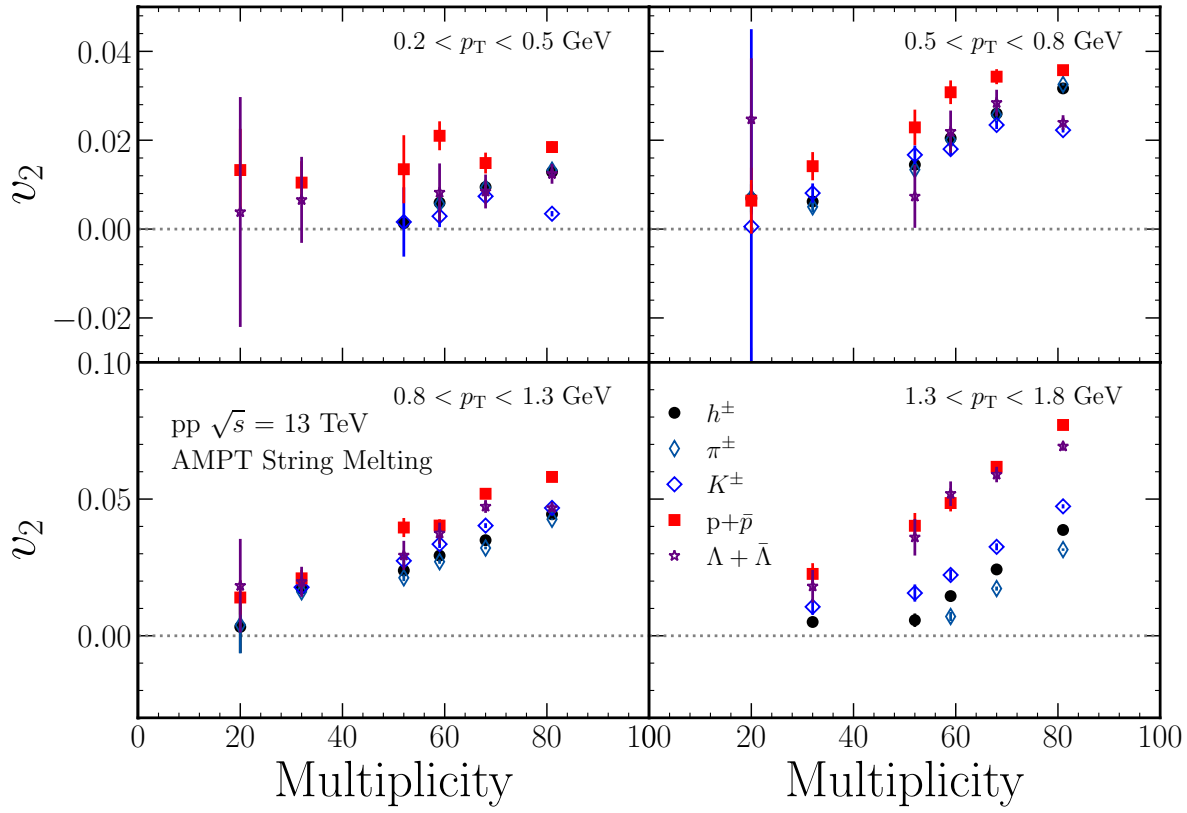

Figure 4.5: Calculated elliptic flow v_2 as function of multiplicity N_{ch}. Shown p_T ranges are from low- and high-p_T regions displaying results for baryons, mesons and unidentified hadrons.

verse momentum. This generates more visible mass ordering and particle type grouping between different type particle flow as function of the multiplicity.

Chapter 5

Conclusions

Flow coefficients from various particle species by using long-range correlations are extracted from four event generators in pp collisions at $\sqrt{s} = 13$ TeV using the LMTF method.

A clear non-flow structure was observed in PYTHIA8 default two-particle correlation function which extended $|\Delta\eta| > 4$ which was used in estimating non-flow in various $\Delta\eta$-regions. It was found that the subtraction of non-flow still introduces kinematic bias coming from jets and also bias from different implementations of flow and non-flow components in used models. Furthermore, it was observed that analysis done to PYTHIA8 default produced biased results toward larger flow. Additionally, EPOS4 and PYTHIA8 string shoving model data had non-flat near-side in low-multiplicity events. This meant that flow extraction couldn't be done due to the unfilled assumptions in the method used in analysis.

Since AMPT string melting showed a flat near-side in low-multiplicity events, it was used in this analysis. Estimation of away-side shape modification was not possible due to that all models, excluding PYTHIA8 default, had both flow and non-flow components implemented in their simulations. Still, when comparing to other models, away-side shapes from other models were more concentrated around $\Delta\varphi \approx \pi$ where as AMPT showed lower yield and broader ridge structure. Also, as the analysis showed that models, other than AMPT string melting, exhibited bias from non-flow even with gap-D, there is a possibility of jet contamination with the current ALICE η acceptance.

The results from AMPT string melting showed multiplicity dependent particle type grouping and mass ordering at high-p_T. Figures from quark-number scaled v_2 as function of transverse kinetic energy displayed results that were different from large systems studies.

Bibliography

[1] R. Pasechnik and M. Šumbera, "Phenomenological Review on Quark–Gluon Plasma: Concepts vs. Observations," *Universe* **3** no. 1, (2017) 7, arXiv:1611.01533 [hep-ph].

[2] J. Adams *et al.*, "Experimental and theoretical challenges in the search for the quark–gluon plasma: The star collaboration's critical assessment of the evidence from rhic collisions," *Nuclear Physics A* **757** no. 1, (2005) 102–183. https://www.sciencedirect.com/science/article/pii/S0375947405005294. First Three Years of Operation of RHIC.

[3] **CMS** Collaboration, V. Khachatryan *et al.*, "Observation of Long-Range Near-Side Angular Correlations in Proton-Proton Collisions at the LHC," *JHEP* **09** (2010) 091, arXiv:1009.4122 [hep-ex].

[4] J. L. Nagle and W. A. Zajc, "Small System Collectivity in Relativistic Hadronic and Nuclear Collisions," *Ann. Rev. Nucl. Part. Sci.* **68** (2018) 211–235, arXiv:1801.03477 [nucl-ex].

[5] **MADAI** Collaboration, H. Petersen and J. Bernhard.

[6] T. Schäfer and D. Teaney, "Nearly Perfect Fluidity: From Cold Atomic Gases to Hot Quark Gluon Plasmas," *Rept. Prog. Phys.* **72** (2009) 126001, arXiv:0904.3107 [hep-ph].

[7] J. E. Bernhard, J. S. Moreland, S. A. Bass, J. Liu, and U. Heinz, "Applying bayesian parameter estimation to relativistic heavy-ion collisions: Simultaneous characterization of the initial state and quark-gluon plasma medium," *Phys. Rev. C* **94** (Aug, 2016) 024907. https://link.aps.org/doi/10.1103/PhysRevC.94.024907.

[8] S. A. B. U. Jonah E. Bernhard(Duke U.), J. Scott Moreland(Duke U.), "Bayesian estimation of the specific shear and bulk viscosity of quark–gluon plasma," *Nature Phys.* **15** (2019) 1113–1117. https://www.nature.com/articles/s41567-019-0611-8.

[9] W. Li, "Observation of a 'Ridge' correlation structure in high multiplicity proton-proton collisions: A brief review," *Mod. Phys. Lett. A* **27** (2012) 1230018, arXiv:1206.0148 [nucl-ex].

[10] **CMS** Collaboration, S. Chatrchyan *et al.*, "Observation of Long-Range Near-Side Angular Correlations in Proton-Lead Collisions at the LHC," *Phys. Lett. B* **718** (2013) 795–814, arXiv:1210.5482 [nucl-ex].

[11] **CMS** Collaboration, V. Khachatryan *et al.*, "Evidence for collectivity in pp collisions at the LHC," *Phys. Lett. B* **765** (2017) 193–220, arXiv:1606.06198 [nucl-ex].

[12] **STAR** Collaboration, J. Adams *et al.*, "Experimental and theoretical challenges in the search for the quark gluon plasma: The STAR Collaboration's critical assessment of the evidence from RHIC collisions," *Nucl. Phys. A* **757** (2005) 102–183, arXiv:nucl-ex/0501009.

[13] R. Field, "Min-Bias and the Underlying Event at the LHC," *Acta Phys. Polon. B* **42** (2011) 2631–2656, arXiv:1110.5530 [hep-ph].

[14] **LHCb** Collaboration, R. Aaij *et al.*, "Centrality determination in heavy-ion collisions with the LHCb detector," *JINST* **17** no. 05, (2022) P05009, arXiv:2111.01607 [nucl-ex].

[15] **ALICE** Collaboration, "The ALICE experiment – A journey through QCD," arXiv:2211.04384 [nucl-ex].

[16] S. A. Voloshin, "Anisotropic flow," *Nucl. Phys. A* **715** (2003) 379–388, arXiv:nucl-ex/0210014.

[17] I. Selyuzhenkov and S. Voloshin, "Effects of non-uniform acceptance in anisotropic flow measurement," *Phys. Rev. C* **77** (2008) 034904, arXiv:0707.4672 [nucl-th].

[18] A. M. Poskanzer and S. A. Voloshin, "Methods for analyzing anisotropic flow in relativistic nuclear collisions," *Phys. Rev. C* **58** (1998) 1671–1678, arXiv:nucl-ex/9805001.

[19] **ALICE** Collaboration, "Multiplicity dependence of jet-like two-particle correlation structures in p–pb collisions at snn=5.02 tev," *Physics Letters B* **741** (2015) 38–50. https://www.sciencedirect.com/science/article/pii/S0370269314008302.

[20] Z.-W. Lin, C. M. Ko, B.-A. Li, B. Zhang, and S. Pal, "A Multi-phase transport model for relativistic heavy ion collisions," *Phys. Rev. C* **72** (2005) 064901, arXiv:nucl-th/0411110.

[21] S. Ji, M. Virta, T. Kallio, S. H. Lim, and D. J. Kim, "Toward unbiased flow measurements in *pp* collisions at the cern large hadron collider," *Phys. Rev. C* **108** (Sep, 2023) 034909. https://link.aps.org/doi/10.1103/PhysRevC.108.034909.

[22] J. Kim, E.-J. Kim, S. Ji, and S. Lim, "Exploring the string shoving model in Pythia8 for collective behaviors in pp collisions," *J. Korean Phys. Soc.* **79** no. 5, (2021) 447–454, arXiv:2108.09686 [nucl-th].

[23] **CMS** Collaboration, V. Khachatryan *et al.*, "Measurement of long-range near-side two-particle angular correlations in *pp* collisions at $\sqrt{s} = 13$ TeV," *Phys. Rev. Lett.* **116** (Apr, 2016) 172302. https://link.aps.org/doi/10.1103/PhysRevLett.116.172302.

[24] B. B. Back, "Studies of multiplicity in relativistic heavy-ion collisions," *Journal of Physics: Conference Series* **5** no. 1, (Jan, 2005) 1. https://dx.doi.org/10.1088/1742-6596/5/1/001.

[25] P. Parfenov, D. Idrisov, V. B. Luong, and A. Taranenko, "Relating charged particle multiplicity to impact parameter in heavy-ion collisions at nica energies," *Particles* **4** no. 2, (2021) 275–287. https://www.mdpi.com/2571-712X/4/2/24.

[26] M. Aaboud *et al.*, "Correlated long-range mixed-harmonic fluctuations measured in pp, p+pb and low-multiplicity pb+pb collisions with the atlas detector," *Physics Letters B* **789** (2019) 444–471. https://www.sciencedirect.com/science/article/pii/S0370269318309948.

[27] **ATLAS** Collaboration, "Measurement of long-range pseudorapidity correlations and azimuthal harmonics in $\sqrt{s_{NN}} = 5.02$ tev proton-lead collisions with the atlas detector," *Phys. Rev. C* **90** (Oct, 2014) 044906. https://link.aps.org/doi/10.1103/PhysRevC.90.044906.

[28] **ALICE** Collaboration, J. Adam *et al.*, "Centrality dependence of particle production in p-Pb collisions at $\sqrt{s_{\rm NN}}$= 5.02 TeV," *Phys. Rev. C* **91** no. 6, (2015) 064905, arXiv:1412.6828 [nucl-ex].

[29] S. Tang, L. Zheng, X. Zhang, and R. Wan, "Investigating the elliptic anisotropy of identified particles in p–Pb collisions with a multi-phase transport model," arXiv:2303.06577 [hep-ph].

Appendix A

Appendix

A.1 Two-particle correlation function preparations

```
1  // <Excluded code>
2
3          hSame = (TH2D *)fin->Get( ... )
4          hMix = (TH2D *)fin->Get( ... );
5
6  // <Excluded code>
7
8          if(icomb == 2) {
9            hTrigg = (TH1D*)fin->Get( ... );
10         } else {
11           hTrigg = (TH1D*)fin->Get( ... );
12         }
13
14         double ntrigg =  hTrigg->Integral(hTrigg->FindBin(pTMin[iptt]),
       hTrigg->FindBin(pTMax[iptt]));
15
16 // <Excluded code>
17
18           double normMix = hMix->GetMaximum();
19         hMix->Scale(1./normMix);
20
21         hDphiAssoc2D[kReal][k][ic][iptt] = (TH2D *)hSame->Clone();
22         hDphiAssoc2D[kMixed][k][ic][iptt] = (TH2D *)hMix->Clone();
23         hDphiAssoc2D[kSignal][k][ic][iptt] = (TH2D *)hSame->Clone();
24         hDphiAssoc2D[kSignal][k][ic][iptt]->Divide(hMix);
25         hDphiAssoc2D[kSignal][k][ic][iptt]->Scale(1./ntrigg,"width");
26
27 // <Excluded code>
```

Listing A.1: Constructing a two-particle correlation function (see Eq. 2.13). In lines 3-4 and 8-12 same and mixed distributions along with trigger particle counts are loaded into histograms. Then in line 14 histogram holding N_{trig} counts is integrated over some p_T range and saved as a number. Then between lines 18 to 19 a normalized mixed distribution

is generated using a maximum value bin. Then lines 21-25 display a divide of the same event distribution with the normalized mixed event and scaling of each with N_{trig}.

A.2 Projections into $\Delta\varphi$

```
1
2  // <Excluded code>
3
4    for(int k=0; k<NPID; k++){
5      for (int ic = 0; ic < nbins_mult; ic++){
6        for (int iptt = 0; iptt < Nptt; iptt++){
7            for(int ig = 0; ig < Negap; ig++){
8
9              Int_t minBin = ... // Minimum bin
10             Int_t maxBin = ... // Maximum bin
11
12             hLongRangeDeltaphi[k][ic][iptt][ig] =
13             (TH1D*) h2D[k][ic][iptt]->ProjectionX( ... );
14
15 // <Excluded code>
```

Listing A.2: Projecting corrected two-particle correlation plots in lines 12-13 while looping over each configuration of PID and multiplicity and p_T range and $\Delta\eta$-gaps in lines 4-7. Lines 9-10 show calculation for correct η-regions (Negap) from 2D-histograms and saving them as bin numbers for the cut.

A.3 Chi-square testing and finding fitting parameters

```
1  void JLMTemplateFitSingle( ... ) {
2
3  // <Excluded code>
4
5    ROOT::Math::Minimizer *pmin = ROOT::Math::Factory::CreateMinimizer("
       Minuit2","");
6
7  // <Excluded code>
8
9    ROOT::Math::Functor f(&chi2,4);
10   double params[4] = {2,4,0.02,0.02};
11
12   pmin->SetFunction(f);
13
14 // <Excluded code>
15
16   pmin->Minimize();
17
18   Fperi = pmin->X()[0];
19   FperiErr = pmin->Errors()[0];
20   Gperi = pmin->X()[1];
21   GperiErr = pmin->Errors()[1];
22   V2peri = pmin->X()[2];
23   V2periErr = pmin->Errors()[2];
24   V3peri = pmin->X()[3];
25   V3periErr = pmin->Errors()[3];
26   vnn[0] = V2peri;
27   vnnError[0] = V2periErr;
28   vnn[1] = V3peri;
29   vnnError[1] = V3periErr;
30
31 // <Excluded code>
```

Listing A.3: Line 1 shows naming the function for low-multiplicity template fitting. Then in line 5 algorithm makes a Minimizer type reference variable to a static method called Minuit2. Line 9 shows wrapping right-side of the function defined in Eq. 3.1 around a functor class and a setting of parameter size to four. Wrapping is done because the Minuit2 library while able to do multi-parameter analyzing is not able to do multiple iterations simultaneously. Functor-class objects can do simultaneous iterations using so called "virtual cloning" which quickens the analyzing process and thus saves computer processing time. Line 10 and 12 displays declaring parameters for function initializing and setting the function for minimizing. Line 16 is calling the Minimize-method from Minimizer-class to do chi-square testing to the right-side of Eq. 3.1. The chi-square value is then minimized by trying different combinations of values for jet yield related relative factor F and normalization constant G along with $v_{2,2}$ and $v_{3,3}$ parameters. Lastly most fitted parameters along with their errors are saved into variables in lines 18-29.

A.4 Low-multiplicity template fitting

```
1
2
3   hSig_a_G = (TH1D*) hSub->Clone();
4   for (int k = 1; k <= hSig_a_G->GetNbinsX(); k++) {
5       double value = hSig_a_G->GetBinContent(k);
6       value = value*Fperi + Gperi;
7       hSig_a_G->SetBinContent(k, value);
8   }
9
10 // <Excluded code>
11
12     for (Int_t n=0; n<NH; n++){
13     TString formula = Form( ... );
14     fitvnn_s[n]= new TF1( ... );
15     fitvnn_s[n]->Print();
16     fitvnn_s[n]->SetParameter(1, vnn[n]);
17     fitvnn_s[n]->SetParameter(0, Gperi);
18     fitvnn_s[n]->SetParameter(2, ScaleFYmin);
19     fitvnn_s[n]->Write();
20   }
21
22   hFitTotal = (TH1D*) hSub->Clone();
23
24   TString formula = Form( ... );
25   TF1 *fittot= new TF1( ... );
26   fittot->SetParameter(0,Gperi);
27   fittot->SetParameter(1,vnn[0]);
28   fittot->SetParameter(2,vnn[1]);
29
30     for (int k = 1; k <= hSub->GetNbinsX(); k++)
31     {
32         Double_t ylm = hSub->GetBinContent(k);
33         Double_t x = hSub->GetXaxis()->GetBinCenter(k);
34         Double_t tot =  Fperi*ylm + fittot->Eval(x);
35         hFitTotal->SetBinContent(k, tot);
36     }
37 }
```

Listing A.4: Line 3 shows cloning of projected low-multiplicity distribution into another 1D-histogram. Lines 4-8 display generating the scaled and normalized low-multiplicity distribution corresponding to high-multiplicity distribution without flow modulation (see Eq. 3.4). Then creation and saving of the normalized and F scaled low-multiplicity signals as TF1 functions for each harmonic n with chi-square tested parameters are seen in lines 12-20. Another cloning of low-multiplicity distribution is seen in line 23. Generating of v_2 and v_3 curves is done in lines 24-28 and between lines 30 and 36 is created the high-multiplicity distribution.

A.5 Creating graphs for plotting

```
1
2  void makegraphs(TString MC_name, TString comb_name) {
3
4      creategraphs();
5
6  // <Excluded code>
7
8      while ( ... ) {
9          grVnnCentDep[ipid][0][ipt][ig]->SetPoint(ic, xnch[ic] , v2);
10         grVnnCentDep[ipid][0][ipt][ig]->SetPointError(ic, 0, v2_err);
11         grVnnCentDep[ipid][1][ipt][ig]->SetPoint(ic, xnch[ic] , v3);
12         grVnnCentDep[ipid][1][ipt][ig]->SetPointError(ic, 0, v3_err);
13         grVnnpTDep[ipid][0][ic][ig]->SetPoint(ipt, xpt[ipt] , v2);
14         grVnnpTDep[ipid][0][ic][ig]->SetPointError(ipt, 0 , v2_err);
15         grVnnpTDep[ipid][1][ic][ig]->SetPoint(ipt, xpt[ipt] , v3);
16         grVnnpTDep[ipid][1][ic][ig]->SetPointError(ipt, 0 , v3_err);
17     }
18
19 // <Excluded code>
20
21     writegraphsToroot(MC_name, comb_name);
22 }
```

Listing A.5: In line 2 is the naming of a function for creating TGraphError graphs with Monte-Carlo event generator name and detector combination (e.g. TPC-FMDC) as parameters. Line 4 displays a function call for initializing empty TGraphErrors. Then in lines 8-17 is a while-loop which goes through empty graphs and fills them with saved values from LMTF method analysis seen in Listing. A.4. After this graphs are saved for plotting with Python.

Appendix B

Original papers

Toward an unbiased flow measurements in LHC pp collisions

S. Ji[1], M. Virta[2,3], T. Kallio[2], S.H Lim[1], and D.J. Kim[2,3*]
[1] *Pusan National University, Department of Physics, Busan 46241, Republic of Korea*
[2] *University of Jyväskylä, Department of Physics, P.O. Box 35, FI-40014 University of Jyväskylä, Finland*
[3] *Helsinki Institute of Physics, P.O.Box 64, FI-00014 University of Helsinki, Finland*
(Dated: November 3, 2023)

Long-range correlations for pairs of charged particles with two-particle angular correlations are studied in pp at $\sqrt{s} = 13$ TeV with various Monte Carlo generators. The correlation functions are constructed as functions of relative azimuthal angle $\Delta\varphi$ and pseudorapidity separation $\Delta\eta$ for pairs of different particle species with the identified hadrons such as π, K, p, and Λ in wide $\Delta\eta$ ranges. Fourier coefficients are extracted for the long-range correlations in several -multiplicity classes using a low-multiplicity template fit method. The method allows to subtract the enhanced away-side jet fragments in high-multiplicity with respect to low-multiplicity events. However, we found that due to a kinematic bias on jets and differing model implementation of flow and jet components, subtracting the non-flow contamination in small systems can bias the results. It is found that PYTHIA8 default model where the presence of the collective flow is not expected but the bias results in very large flow. Also extracting flow signal from the EPOS4 and PYTHIA8 string shoving models is not possible because of flow signal introduced in the low-multiplicity events. Only a multiphase transport string melting model among studied model calculations is free from this bias, and shows a mass ordering at low $p_{\rm T}$ and particle type grouping in the intermediate $p_{\rm T}$ range. This feature was first observed in large systems, but the mass ordering in small systems differs from that observed in large collision systems.

I. INTRODUCTION

Collisions between heavy-ions (HIC) exhibit strong collectivity, as demonstrated by the anisotropy in the momentum distribution of final particles emitted at the Relativistic Heavy Ion Collider (RHIC) [1–4] and the Large Hadron Collider (LHC) [5–7]. The spatial anisotropies are converted to anisotropies in the final momentum distribution due to a pressure-driven expansion of the strongly interacting quark-gluon plasma (QGP) formed during the collision event. The produced QGP in HIC is in the strongly coupled regime and the state-of-the-art Bayesian analyses utilizing the experimental data favor small values of the shear viscosity to entropy density ratio (η/s), which implies that the produced QGP is considered the fluid with the lowest shear viscosity to entropy density ratio observed in nature [8, 9]. In Recent years, the primary focus has been to constrain model parameters by measuring sensitive observables, using Bayesian analyses [10–15].

To probe the collective behavior in the momentum anisotropy, long-range particle correlations are used over a wide range of pseudorapidity. Over the past few years, long-range correlations have also been observed in smaller collision systems, such as high-multiplicity (HM) proton-proton (pp) collisions [16–20], proton-nucleus (pA) collisions [21–24], and collisions of light ions with heavy ions, such as p+Au, d+Au, ^{3}He+Au [25, 26]. These observations raise the question of whether small system collisions have a similar underlying mechanism for developing correlations as heavy AA collisions.

On the experimental side, extracting flow in small systems remains challenging due to a strong jet fragmentation bias to the long-range correlations. One commonly used approach for suppressing the non-flow contribution in two-particle correlations is to require a large $\Delta\eta$ gap between the two particles, which is also applied in cumulant methods [19, 27]. However, this approach only eliminates non-flow contributions on the near side, not on the away side ($\Delta\varphi \sim \pi$). To address this limitation, a low-multiplicity template fit (LMTF) method has been proposed to remove away-side contributions as well [16, 23, 28], taking into account the autocorrelation between event multiplicity and jet yields [29]. This method enables the subtraction of enhanced away-side jet yields in HM events compared to low-multiplicity (LM) events, and may potentially provide a lower limit on the event multiplicity needed to observe the flow signal.

The observed scaling pattern of the elliptic flow with respect to the number of constituent quarks (NCQ) in large collision systems at RHIC [30–33] and LHC [6, 34–37] suggests the creation of a thermalized bulk system of quarks that coalesce into hadrons. However, it is known that NCQ scaling is an approximate argument and is not expected to be exact. For example, Ref. [38] demonstrates that NCQ scaling is impacted by the initial conditions for the evolution of the parton phase as well as by interactions in the hadronic phase. Another study [39] shows the violation of NCQ scaling due to finite baryon density and high phase-space density of partons [40]. Although the scaling in large collision systems is observed to hold at an approximate level of 20% [36, 37], the question of whether these patterns can still be observed in collisions of small systems is of great current interest.

* su-jeong.ji@cern.ch

Understanding how the NCQ scaling in smaller systems is different from that in large systems would provide important insights into the underlying physics of the system. An approximate NCQ scaling of charged hadrons' v_2 in p–Pb collisions at $\sqrt{s_{\rm NN}}$ = 5.02 TeV is observed at intermediate $p_{\rm T}$ with ALICE [41] and also for v_2 of π and p in ^{3}He+Au collisions at $\sqrt{s_{\rm NN}}$ = 200 GeV with PHENIX [42]. However, this observation was based on a limited range of $p_{\rm T}$ with the cumulant methods and further experimental checks are needed to confirm the presence of NCQ scaling over a wider range of $p_{\rm T}$ with the experimental LMTF method. Additionally, it is important to note that other effects, such as initial-state fluctuations and final-state correlations, can also contribute to the observed elliptic flow in small systems. Therefore, more detailed studies are needed to understand the interplay of these effects and the possible mechanisms underlying the observed NCQ scaling patterns.

On the theoretical side, systematic mapping of the multiparticle correlations across collision systems by varying sizes is presently underway (see e.g. [43]). The quantitative description of the full set of experimental data has not been achieved yet. A summary of various explanations for the observed correlations in small systems is given in [44–46].

Another important piece of evidence for a strongly interacting medium in small collision systems would be the presence of jet quenching [47, 48]. However, no evidence of jet quenching has been observed in either HM pp or p–Pb collisions [49–53]. A study with two-particle angular correlations in short-range correlations around ($\Delta\eta$, $\Delta\varphi$) = (0, 0) is a good tool for studying jet fragmentations [54].

This report investigates the relationship between jet production and collective phenomena in small systems using various Monte Carlo event generators, such as a multiphase transport (AMPT) string melting model [55], PYTHIA8 string shoving [56, 57], and EPOS4 [58]. Although all three models incorporate both jets and collective flow effects, they differ in their approach to describing collective flow. To determine the suitability of each model for a specific experimental method, we assess the latest flow extraction technique, LMTF, against these models. This paper is organized as follows. First, the model descriptions are given in Sec. II and analysis methods are described in Sec. III. The results from model calculations are presented in Sec. IV. Finally, the results are summarized in Sec. V.

II. MODEL DESCRIPTIONS

In this study, several Monte Carlo (MC) event generators, such as PYTHIA8, AMPT, and EPOS4, of different characteristics are used to compare the non-flow subtraction results. We generate a few million pp collision events with each event generator and collect final-state charged particles for further analysis. Here we have a brief description of the event generators.

PYTHIA8: PYTHIA8 is a widely used event generator for high-energy pp collisions, and it recently incorporates a capability of heavy-ion collisions. It includes both hard and soft interactions for jets and underlying events, and the default parameter set called Monash tune can reasonably describe the production of soft particles [59]. In the default version, there is no partonic or hadronic interaction, so we do not expect a long-range correlation among produced particles due to the flow contribution. Hence, it has been used to verify methods to estimate the non-flow contribution [60].

PYTHIA8 string shoving: In PYTHIA8, a model to describe the long-range correlation in HM pp collisions called "string shoving" has been implemented as an option [56, 57]. This model introduces a repulsive force between strings, and the interaction can cause a microscopic transverse pressure, giving rise to the long-range correlations. The string shoving approach in PYTHIA8 successively reproduces the experimental measurements of the long-range near-side ($\Delta\varphi \sim 0$) ridge yield in HM pp events by ALICE [61] and CMS [18]. However, strings produced from hard scatterings are also affected by the repulsive force, which then leads to observed long-range correlation even in low-multiplicity events [62].

AMPT: Besides several models based on the causal hydrodynamic framework in describing the collective evolution in small collision systems, the AMPT model with string melting [55] can reproduce the flow-like signals by modeling the evolution of medium as a collection of interacting quarks and hadrons [63]. The applicability of fluid-dynamical simulations and partonic cascade models in small systems has been explored in Ref. [64]. In the context of kinetic theory with isotropization-time approximation, the model can smoothly explain the long-range correlations by fluid-like (hydrodynamic) excitations for Pb–Pb collisions and particle-like (or non-hydrodynamic) excitations for pp or p–Pb collisions [65–67]. This study uses the parton cross section value of 3 mb, which is the same as the one used in larger system studies [55]. The value of the parton cross sections is crucial as they affect the final state observables.

EPOS4: The EPOS model describe the full evolution of medium produced by heavy-ion collisions with two parts called a core and a corona [68]. The core part follows the hydrodynamic expansion, and the corona part is composed of hadrons from string decays. After the hadronization process of the core part, the UrQMD model is used to describe hadronic interactions among all hadrons from two parts. The version called EPOS LHC including a different type of radial flow in the case of a small but a very dense system can successfully describe the long-range correlation in HM pp events [61]. Recently, a new version of EPOS (EPOS4) has been released to the public. We utilize the framework for this study.

The summary of the model characteristics is listed in Tab. I. The PYTHIA8 default model is used to under-

Models	Characteristics	Mechanism
PYTHIA8 default	jets and no flow	Ref. [59]
PYTHIA8 shoving	jets and flow	String repulsion [56, 57]
AMPT	jets and flow	String melting[55]
EPOS4	jets and Hydro	Core (hydrodynamical) [58]

TABLE I. A list of the models used in this paper.

stand the non-flow contributions. The PYTHIA8 string shoving, AMPT, and EPOS4 models all include both jets and collective flow effects. However, they differ in their mechanisms for describing the collective flow. It is important to note that the applicability of each model to a specific experimental method may depend on various factors, such as the collision system being studied, as well as the specific observables being measured. Therefore, it is important to carefully consider the strengths and limitations of each model when interpreting experimental results. For instance, in the study by the ALICE Collaboration [61], both PYTHIA8 string shoving and EPOS4 fail to reproduce the near-side jet yields, with PYTHIA8 string shoving predicting an increasing near-side jet yield with increasing multiplicity, while EPOS4 shows the opposite trend. Regarding the ridge yields, EPOS4 overestimates them, while PYTHIA8 string shoving underestimates them. The ridge yields in low multiplicity events are similar to those in HM events for EPOS4 and PYTHIA8 string shoving, while they decrease towards low multiplicity events in the experimental data [17].

III. ANALYSIS PROCEDURE

A. Event and particle selections

This analysis uses the same event selection criteria as the ALICE experiments, which require a charged particle in both V0A and V0C [70, 71] acceptance. The V0A and V0C cover the pseudorapidity ranges $2.8 < \eta < 5.1$ and $-3.7 < \eta < -1.7$, respectively. The contribution from diffractive interactions is minimized in these events [69]. Fig. 1 shows the charged particle density in various $p_{\rm T}$ intervals. Every model describes the trend of the data well, while PYTHIA8 string shoving and AMPT model overestimates the data from the ALICE Collaboration [69]. Despite of PYTHIA8 string shoving model largely overestimates the data, the $p_{\rm T}$ dependency is similar with PYTHIA8 default and EPOS4. In the case of the AMPT model, it shows the different $p_{\rm T}$ dependency.

The multiplicity percentiles are estimated by V0M, which is the sum of the charged particles both in the V0A and V0C acceptance. The event multiplicity of V0M from different generators is shown in Fig. 2. PYTHIA8 string shoving model generates HM events more than other models. The vertical lines indicates the 0–5%, 5–20% and 60–100% event multiplicity of AMPT string melting events. For the identified flow measurement, π, K, and p for all models and additionally Λ for AMPT

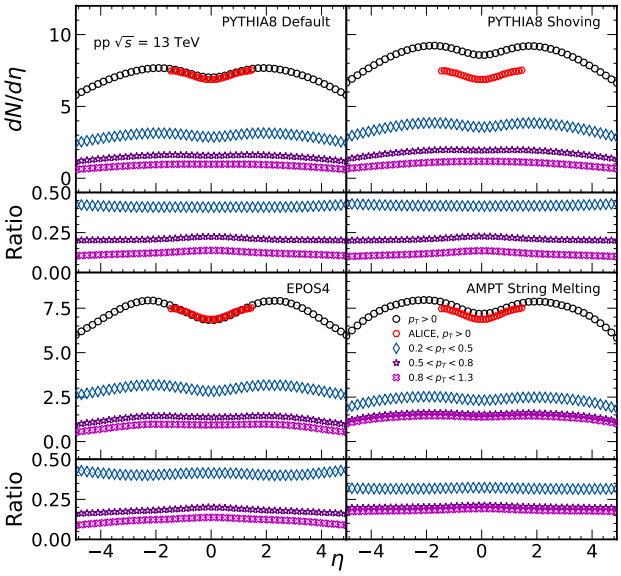

FIG. 1. Charged–particle pseudorapidity density for four different $p_{\rm T}$ intervals over a broad η ranges in several model calculations is compared to the ALICE data [69].

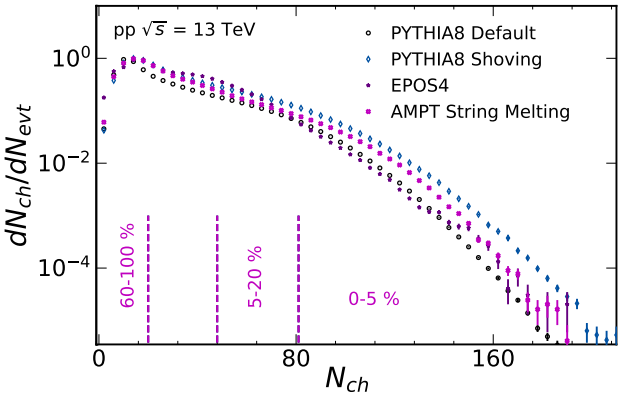

FIG. 2. The distribution of the V0M charged particles in the region $-3.7 < \eta < -1.7$ and $2.8 < \eta < 5.1$. This is used to determine the event multiplicity classes in pp collisions at $\sqrt{s} = 13$ TeV.

model are studied by selecting the particle identification code from the models in the range of $0.2 < p_{\rm T} < 6$ GeV/c.

B. Two-particle angular correlations

Two-particle angular correlations are measured as functions of the relative azimuthal angle ($\Delta\varphi$) and the relative pseudorapidity ($\Delta\eta$) between a trigger and associated particles

$$\frac{1}{N_{\rm trig}}\frac{{\rm d}^2N_{\rm pair}}{{\rm d}\Delta\eta{\rm d}\Delta\varphi} = B_{max}\frac{S(\Delta\eta,\Delta\varphi)}{B(\Delta\eta,\Delta\varphi)}\Big|_{p_{\rm T,\,trig},\,p_{\rm T,\,assoc}}, \quad (1)$$

where the trigger and associated particles are defined for different transverse momentum ranges and different η acceptance of the detectors. The $N_{\rm trig}$ and $N_{\rm pair}$ are the numbers of trigger particles and trigger-associated particle pairs, respectively. $S(\Delta\eta, \Delta\varphi)$ corresponds to the average number of pairs in the same event and $B(\Delta\eta, \Delta\varphi)$ to the number of pairs in mixed events. B_{max} represents the normalization of $B(\Delta\eta, \Delta\varphi)$, and by dividing $S(\Delta\eta, \Delta\varphi)$ with $B(\Delta\eta, \Delta\varphi)/B_{max}$ the acceptance effects are corrected for. This analysis is performed for several multiplicity percentiles (0–5%, 0–20%, 20–40%, and 60–100%), and for each multiplicity percentile.

The flow studies using the ALICE detector were carried out using only the particles detected in the time projection chamber (TPC) detector [69]. However, due to the limited η acceptance of the TPC detector, the study was restricted to the edge of the detector with $1.6 < \Delta\eta| < 1.8$, as well as $p_{\rm T} > 1.0$ GeV/c to avoid non-flow contributions [69]. To further suppress non-flow contributions, preliminary studies by the ALICE experiment have used the forward multiplicity detectors (FMD) to achieve a large η separation of the correlated particles, up to $|\Delta\eta| \approx 6$. In this analysis, we use the same combinations of correlations between particles in the TPC and FMD detectors.

Tab. II lists the η acceptance and measurable $p_{\rm T}$ ranges for each detector used in the analysis.

Detector	η acceptance	$p_{\rm T}$ range
TPC	$\|\eta\| < 0.8$	$0.2 < p_{\rm T} < 6.0$ GeV/c
FMDA	$1.9 < \eta < 4.8$	$p_{\rm T} > 0.0$ GeV/c
FMDC	$-3.1 < \eta < -1.9$	$p_{\rm T} > 0.0$ GeV/c

TABLE II. The acceptance of the detectors used for the trigger and/or associated particles.

As for TPC–FMD correlations, the trigger particles are from TPC detectors with various $p_{\rm T}$ intervals and the associated particles are from forward multiplicity detector A (FMDA) or from forward multiplicity detector C (FMDC) in a different η ranges with $p_{\rm T} > 0.0$ GeV/c. As for FMDA–FMDC correlations, both trigger and associated particles come from FMD detector with $p_{\rm T} > 0.0$ GeV/c. The $\Delta\eta$ ranges used for the default analysis with the full η acceptance of all detectors and four additional wider $\Delta\eta$ gaps used to further reduce the non-flow contributions are summarized in Tab. III.

Correlations	Default	Gap-A	Gap-B	Gap-C	Gap-D
TPC-FMDA	[1.1, 5.6]	[1.5, 5.6]	[2.0, 5.6]	[2.5, 5.6]	[3.0, 5.6]
TPC-FMDC	[1.1, 3.9]	[1.6, 3.9]	[2.0, 3.9]	[2.5, 3.9]	[3.0, 3.9]
FMDA-FMDC	[3.8, 7.9]	[4.3, 7.9]	[4.8, 7.9]	[5.3, 7.9]	[5.8, 7.9]

TABLE III. The $|\Delta\eta|$ ranges of each correlation function and four additional wider $\Delta\eta$ gaps used to further reduce the non-flow contributions.

Fig. 3 and Fig. 4 show the 2-dimensional correlation function of each detector combination with the events from PYTHIA8 default and AMPT string melting models, respectively. Unlike the events from AMPT having both flow and jet components, the PYTHIA8 default events contain the particles purely from jets. The peak seen in the short-range represents the jet contribution. Even though already having long-range correlations by using the particles in TPC and FMD, still the large jet contamination is seen. To find a safe long-range region for the analysis, five different long-ranges are selected to study the effect on the degree of the jet contamination. Different shape and the amplitude of the jet peak is seen depending on the models.

In the next section, the details about the LMTF method, which is used for the non-flow subtraction, will be discussed as well as the assumptions of the method.

C. Extraction of flow coefficients from the Low-Multiplicity Template Fit Method

Due to the strong jet fragmentation bias in small collision systems it is difficult to extract the flow in these collisions because of the remaining non-flow in the away-side region ($\Delta\varphi \sim \pi$) in Eq. 1. As discussed in Refs. [16, 23], the HM correlation function in a HM percentile can be expressed as

$$\begin{aligned} Y_{\rm HM}(\Delta\varphi) = G\ (1 &+ 2v_{2,2}\cos(2\Delta\varphi) \\ &+ 2v_{3,3}\cos(3\Delta\varphi) \\ &+ 2v_{4,4}\cos(4\Delta\varphi)) \\ &+ F\ Y_{\rm LM}(\Delta\varphi) \quad , \end{aligned} \tag{2}$$

where $Y_{\rm LM}(\Delta\varphi)$ is the LM correlation function, G is the normalization factor for the Fourier component up to the fourth harmonic, and the scale factor F corresponds to the relative away-side jet-like contribution with respect to the low-multiplicity (LM) (the 60–100%). This method assumes that $Y_{\rm LM}$ does not contain a peak in the near side originating from jet fragmentation and that the jet shape remains unchanged in HM events compared to LM events. The first assumption is well-verified using the selected LMTF for the experimental data [28], while the second assumption regarding the modification of jet shapes is tested using the near-side $\Delta\eta$ distributions. Additionally, the ATLAS Collaboration's study of HM pp and p–Pb collisions in Ref. [28] provides further support for this assumption, as there is no evidence of jet quenching in these collisions [49–53]. The fit determines the scale factor F and pedestal G, and $v_{n,n}$ are calculated from a Fourier transform. It is worthwhile noting that this method does not rely on the zero yield at minimum (ZYAM) hypothesis to subtract an assumed flat combinatorial component from the LMTF as done previously in Refs. [22, 72]. Whether or not if the models agree on the assumption about the jet shape modification depending on the event multiplicity will be discussed in the Sec. IV.

Fig. 5 shows the LMTF results of TPC-FMDA correlation for 0–20% multiplicity percentile from the AMPT

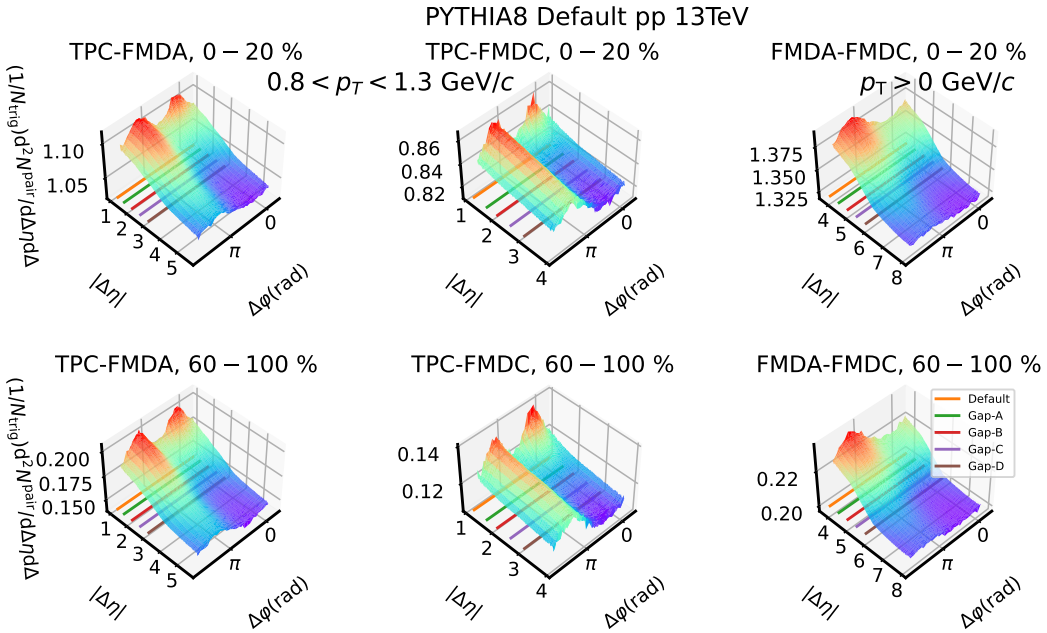

FIG. 3. Two-particle correlation functions as functions of $\Delta\eta$ and $\Delta\varphi$ for HM (0–20%, top panels) and LM (60–100%, bottom panels) events using different combinations of the detectors in $\sqrt{s} = 13$ TeV pp collisions from AMPT string melting calculations. The intervals of $p_{\mathrm{T,\,trig}}$ and $p_{\mathrm{T,\,assoc}}$ are $0.8 < p_{\mathrm{T}} < 1.3$ GeV/c with TPC and $p_{\mathrm{T}} > 0$ GeV/c with FMDA or FMDC.

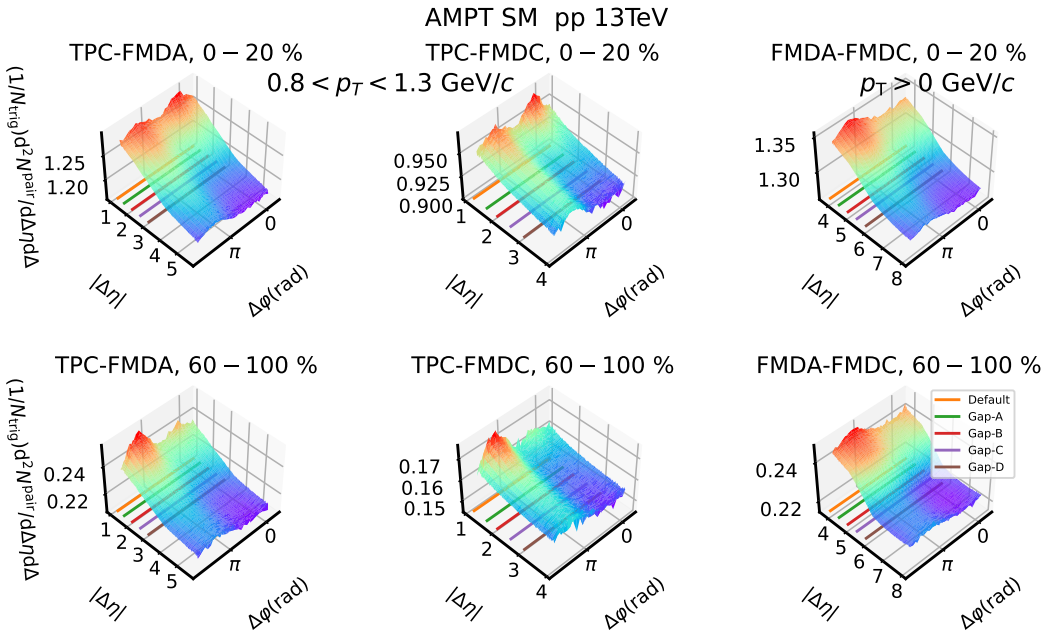

FIG. 4. Two-particle correlation functions as functions of $\Delta\eta$ and $\Delta\varphi$ for HM (0–20%, top panels) and LM (60–100%, bottom panels) events using different combinations of the detectors in $\sqrt{s} = 13$ TeV pp collisions from PYTHIA8 default calculations. The intervals of $p_{\mathrm{T,\,trig}}$ and $p_{\mathrm{T,\,assoc}}$ are $0.8 < p_{\mathrm{T}} < 1.3$ GeV/c with TPC and $p_{\mathrm{T}} > 0$ GeV/c with FMDA or FMDC.

string melting configuration. Even with the default $\Delta\eta$ gap, no ridge structure on the near side is seen in LM correlation function, which indicates that there is almost no jet contamination. The figure also shows the $v_{2,2}$ and $v_{3,3}$ components, yet the $v_{2,2}$ component is dominant.

The low-multiplicity templates of each $\Delta\eta$ gap are seen

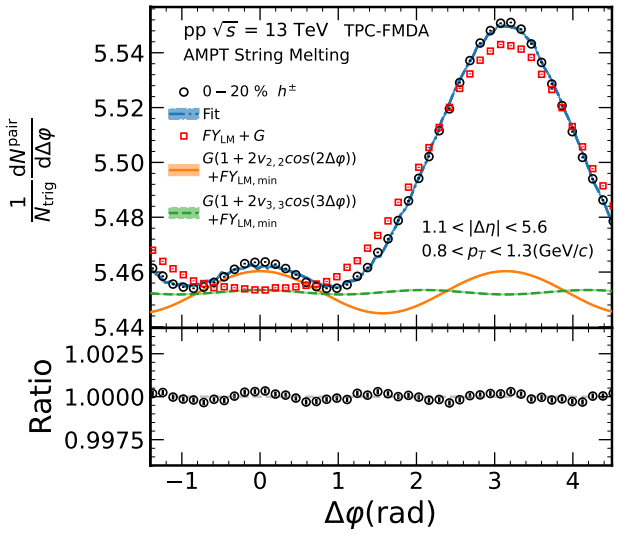

FIG. 5. The low-multiplicity template fit results. The black markers shows the signal for the 0–20% multiplicity percentile together with its fit shown as a blue band. The red squares correspond to the low-multiplicity template. The orange and green curves correspond to the extracted v_2 and v_3 signals, respectively.

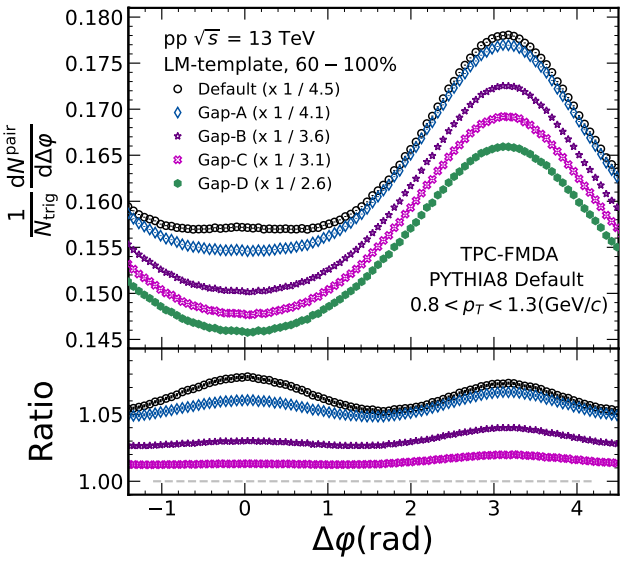

FIG. 6. The $\Delta\eta$ gap dependent low-multiplicity templates with PYTHIA8 default.

in Fig. 6. As the jet shape is well described in PYTHIA8 default, the comparison is done using the PYTHIA8 model. Each template is normalised by its $\Delta\eta$. Decreasing near-side yield is seen with increasing $\Delta\eta$ gap (from default gap to gap-D), and almost the same feature is seen in gap-C and gap-D. Under the first assumption of the template fit method, which requires no near-side yield in the low-multiplicity events, we selected the gap-D for the precise analysis. To see if the other models meet the assumption, the low-multiplicity templates of each model are compared in gap-D.

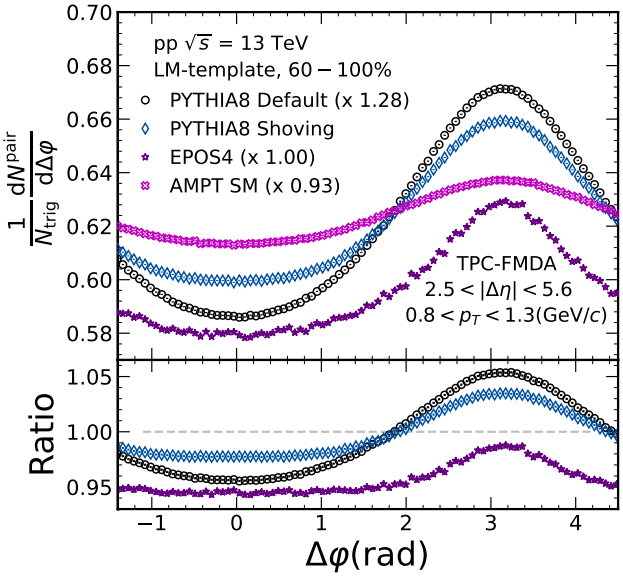

FIG. 7. The LM template for the different model calculations using the default gap.

The comparison between the low-multiplicity templates of each model in the default $\Delta\eta$ gap is seen in the Fig. 7. As the near-side yield in the LM events comes from the jets, there should be no near-side ridge yield for the precise nonflow subtraction. The presence of the LM jet bias indicates that there is a chance of the jet shape modification in the away-side. The ratio is calculated by dividing the AMPT string melting from the PYTHIA8 default, PYTHIA8 string shoving and the EPOS4 models. The PYTHIA8 shows a small near-side yield and the string shoving shows larger yield, whilst there is no ridge yield from the AMPT string melting and the EPOS4 models. In the case of the away-side yield, fairly broad shape is seen in the AMPT string melting version and narrow shape in EPOS4 compared to both PYTHIA8 configurations.

However, we can not test whether the models agree with the second assumption requiring no jet shape modification depending on the event multiplicity. As every model apart from the PYTHIA8 default contains the flow components in the away-side, we can not disentangle the flow and jets.

Finally, v_n are extracted, based on the observed factorization of $v_{n,n}$ to single harmonics [16, 23], using the following equation,

$$v_n(p_{\mathrm{T,TPC}}) = \sqrt{\frac{v_{n,n}^{\mathrm{TPC-FMDA}} \cdot v_{n,n}^{\mathrm{TPC-FMDC}}}{v_{n,n}^{\mathrm{FMDA-FMDC}}}}, \qquad (3)$$

where $v_{n,n}(p_{\mathrm{T,trig}}$ and $p_{\mathrm{T,assoc}})$ are measured in $0.2 < p_{\mathrm{T,trig}} < 6$ GeV/c and integrated p_{T} ranges.

IV. RESULTS

A. Unidentified charged hadron flow

The p_{T}-differential v_2 of the charged particles for different $\Delta\eta$ gap intervals in pp collisions at $\sqrt{s} = 13$ TeV are shown in Fig. 8 for several model calculations. The top panel shows the final v_2 and bottom two row panels show $v_{2,2}$ measured from TPC-FMDA and TPC-FMDC, respectively. The results for PYTHIA8 default are shown in the first column, PYTHIA8 string shoving in the second, EPOS4 in the third, and AMPT string melting on the last. Even though the PYTHIA8 default does not contain any flow component, non-zero v_2 is seen in every $\Delta\eta$ gap. As the $\Delta\eta$ gap becomes larger, the less non-flow dominant region we contain as shown in the Fig. 3, therefore smaller amplitude of v_2 is seen with increasing $\Delta\eta$ gap. Despite the PYTHIA8 string shoving having both flow and non-flow components, similar behavior is observed with the PYTHIA8 default, albeit with a smaller magnitude of the flow component overall. This can be due to the presence of the near-side yield in the low multiplicity which can be seen in the LM-template fit results. In the case of the EPOS4, which also includes the flow components, smaller magnitude of v_2 and $v_{2,2}$ are seen compared to the both PYTHIA8 configurations and similar p_{T} and $\Delta\eta$ gap dependence is seen with PYTHIA8. Lastly, the AMPT string melting model shows that in low p_{T} regions v_2 doesn't vary much on the $\Delta\eta$ gap selection. However, v_2 increases with increasing $\Delta\eta$ gap in contrast to other models. This is mostly due to the fact that the TPC-FMDC correlations are influenced by jet contamination in smaller $\Delta\eta$ gap selections, as seen in the bottom panel of AMPT. In the low p_{T} regions, v_2 are increased by 50 % and in high p_{T} regions, a factor of two respectively. Since the largest $\Delta\eta$ gap has the smallest contribution from non-flow, in latter sections, only results from the AMPT string melting with the gap-D will be shown.

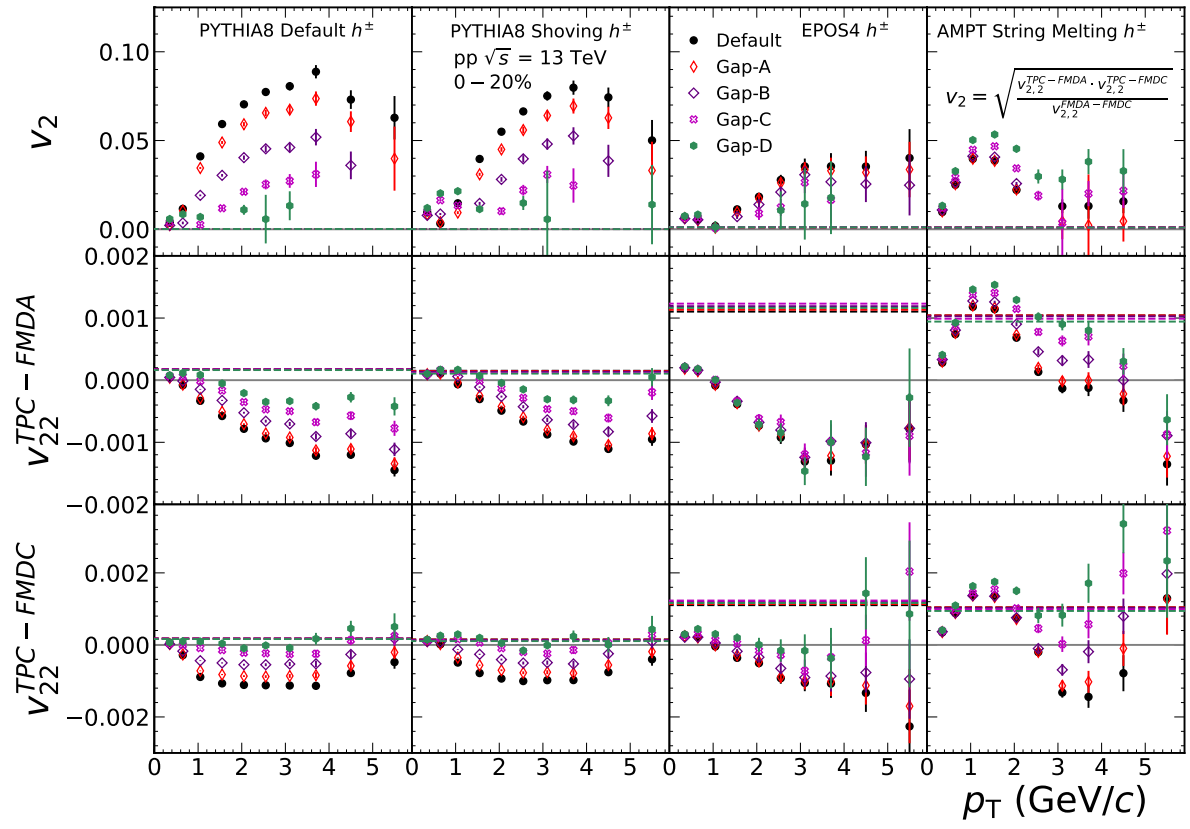

FIG. 8. The p_{T}-differential v_2 for different $\Delta\eta$ gap intervals at $\sqrt{s} = 13$ TeV for several model calculations are shown for the charged particles. Two components to calculate the final v_2 on the top are shown in the bottom two panels. The results of $v_{2,2}^{\mathrm{FMDA-FMDC}}$ and $v_2^{\mathrm{FMDA-FMDC}}$ are shown as dashed lines on each panel.

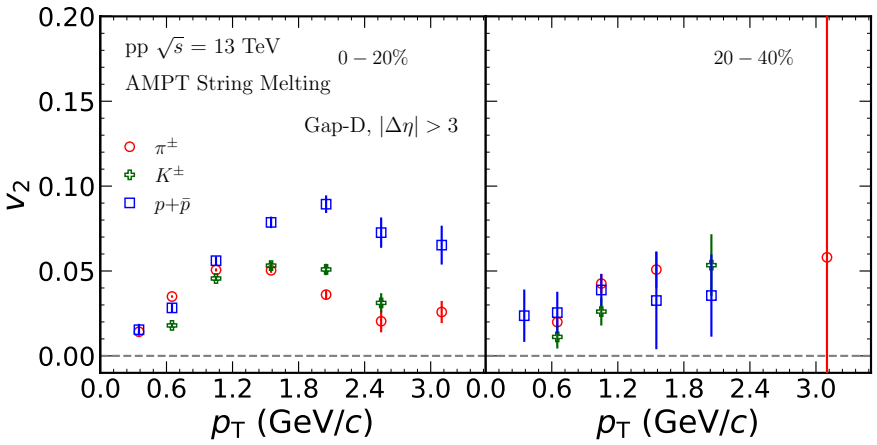

FIG. 9. The p_T-differential v_2 for different particle species in 0–20% and 20–40% multiplicity percentiles in pp collisions at $\sqrt{s}$ = 13 TeV from the AMPT string melting model calculations.

B. Identified charged hadron flow

Fig. 9 shows the v_2 of the identified charged particles in 0–20% and 20–40% events with the AMPT string melting model. Grouping of v_2 is seen depending on the particle species, especially whether the particle is meson or baryon in 0–20% events. In the case of the 20–40% events, the mass splitting is not clearly seen mostly due to the lack of the statistics. Also, as the smaller v_2 is seen in 20–40% compared to 0–20%, we also studied about the multiplicity dependence of v_2.

Fig. 10 shows the dependence of v_2 on transverse kinetic energy, normalized by the number of quark constituents (n_q), using the AMPT string melting model. In the model, the flow of the identified particle is a result of partonic interactions. This leads to mass ordering in the low p_T region of the hadrons and baryon/meson grouping in the intermediate p_T region. The results are also presented as a function of transverse kinetic energy, KE_T. This quantity is defined as $KE_T = m_T - m_0$, where $m_T = \sqrt{m_0^2 + p_T^2}$ is the transverse mass. v_2 and KE_T are then normalized by n_q, as the number of quarks in a particle varies by its type. While previous data from large collision systems at LHC show that the flow coefficients approximately lie on a line regardless of the particle species [6, 34–36], the AMPT results in pp collisions show some deviation from the scaling in both 0–20% (left) and 0–5% (right) events. The ratios on the proton results in pp collisions from the AMPT calculations are very different from what is seen in the large-system collisions in both the experimental data and AMPT calculations (see the supplementary material [73]). Experimental results obtained with the LMTF method over a wider range of p_T will provide further insight into the presence of NCQ scaling in small system collisions.

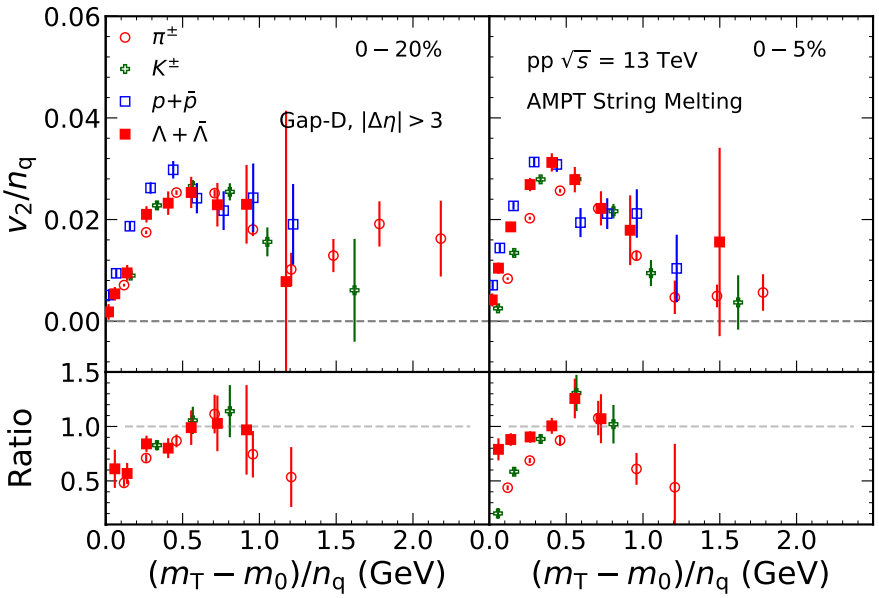

FIG. 10. The NCQ scaled m_T-dependent v_2 for different particle species in 0–20% (left) and 0–5% (right) high multiplicity percentiles in pp collisions at $\sqrt{s} = 13$ TeV from the AMPT string melting model calculations. The ratios to proton results are shown in the bottom panel.

C. Multiplicity dependent flow

In Fig. 11, we present the magnitude of v_2 as a function of multiplicity for various particle species in two p_T ranges. The $|\Delta\eta|$ range considered is > 3, and v_2 is shown for $0.8 < p_T < 1.3, \text{GeV}/c$ and $1.3 < p_T < 1.8, \text{GeV}/c$. Firstly, we observe that the magnitude of v_2 increases with increasing multiplicity for both p_T ranges, regardless of the particle type. Secondly, v_2 decreases towards lower multiplicities and starts to saturate at a multiplicity of around 50. While the AMPT string melting model shows a linear multiplicity dependence, the experimental results reported in Refs. [16, 17, 23] show a mild decrease towards low multiplicity events.

In the case of the higher p_T range shown in the bottom panel of Fig. 11, we observe that the multiplicity dependence of charged hadrons differs from that of identified mesons in the first two multiplicity bins. Interestingly, baryons do not show this saturation yet in those multiplicity ranges, within the uncertainties. Furthermore, the ordering in the v_2 magnitudes between different particle species is visible, as discussed in the previous section. For both p_T ranges, the magnitudes of v_2 are clearly separated between mesons and baryons in higher multiplicities.

V. CONCLUSIONS

We extracted flow coefficients for various particle species, including π, K, p, and Λ, with identified hadrons using a few MC generators and detector combinations in wide $\Delta\eta$ ranges for pp collisions at $\sqrt{s} = 13$ TeV. The flow measurements were obtained through long-range correlations in different high-multiplicity classes by employing the LMTF method. This approach enabled us to eliminate the enhanced away-side jet fragments in high-multiplicity events relative to low-multiplicity events. However, we found that subtracting non-flow contamination in small systems could lead to biased results, due to the kinematic bias on jets and different model implementations of flow and jet components. Specifically, we observed that the PYTHIA8 default model, which does not account for collective flow, produces biased results towards large flow. Moreover, it was not possible to extract flow signals from the EPOS4 and PYTHIA8 string shoving models, which contain flow components, as they violate the assumptions of the LM-template fit method, containing near-side yield in low-multiplicity events. We conducted studies with the LMTF method in multiple $\Delta\eta$-gaps and found that the current ALICE η acceptance might still be influenced by non-flow contamination, suggesting the need for larger $\Delta\eta$-gaps in future analyses. Only the AMPT string melting model among the studied models was free from this bias and showed a mass ordering at low p_T and particle type grouping in the intermediate p_T range, similar to what is observed in large systems. However, this ordering was quite distinct from that seen in large systems.

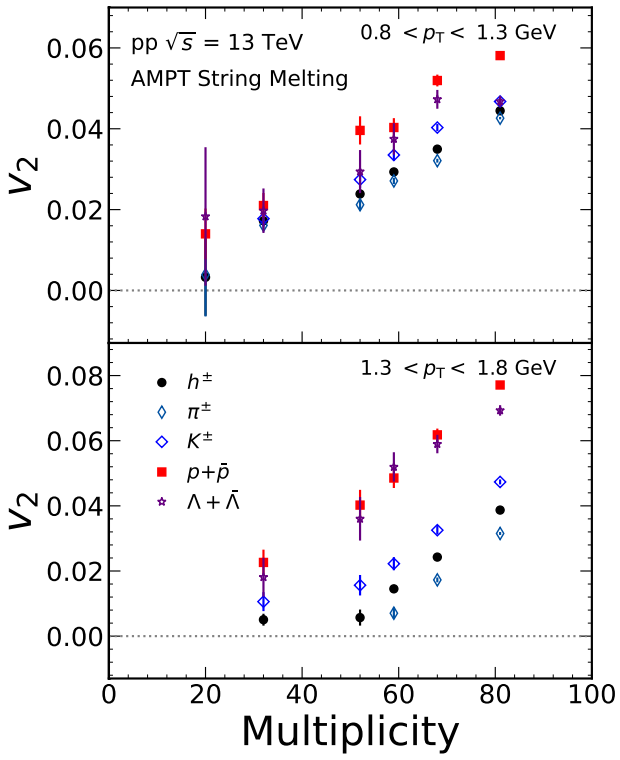

FIG. 11. The multiplicity dependence of v_2 for different particle species in pp collisions at $\sqrt{s} = 13$ TeV from the AMPT string melting model calculations.

ACKNOWLEDGMENTS

We thank Klaus Werner, Christian Bierlich and Zi-Wei Lin for fruitful discussions with their model calculations. We acknowledge CSC - IT Center for Science in Espoo, Finland, for the allocation of the computational resources. MV, TK, and DJK are supported by the Academy of Finland, the Centre of Excellence in Quark Matter (project 346328). SJ and SHL are supported by the National Research Foundation of Korea (NRF) grant funded by the Korea government (MSIT) under Contract No. 2020R1C1C1004985. We also acknowledge technical support from KIAF administrators at KISTI.

[1] J. Adams *et al.* (STAR), Nucl. Phys. A **757**, 102 (2005), arXiv:nucl-ex/0501009.
[2] K. Adcox *et al.* (PHENIX), Nucl. Phys. A **757**, 184 (2005), arXiv:nucl-ex/0410003.
[3] I. Arsene *et al.* (BRAHMS), Nucl. Phys. A **757**, 1 (2005), arXiv:nucl-ex/0410020.
[4] B. B. Back *et al.* (PHOBOS), Nucl. Phys. A **757**, 28 (2005), arXiv:nucl-ex/0410022.
[5] B. Abelev *et al.* (ALICE), Phys. Lett. B **719**, 18 (2013), arXiv:1205.5761 [nucl-ex].
[6] B. B. Abelev *et al.* (ALICE), JHEP **06**, 190 (2015), arXiv:1405.4632 [nucl-ex].
[7] G. Aad *et al.* (ATLAS), Phys. Lett. B **707**, 330 (2012), arXiv:1108.6018 [hep-ex].
[8] P. Kovtun, D. T. Son, and A. O. Starinets, Phys. Rev. Lett. **94**, 111601 (2005), arXiv:hep-th/0405231.
[9] J. E. Bernhard, J. S. Moreland, and S. A. Bass, Nature Physics (2019), 10.1038/s41567-019-0611-8.
[10] J. Auvinen, K. J. Eskola, P. Huovinen, H. Niemi, R. Paatelainen, and P. Petreczky, Phys. Rev. C **102**, 044911 (2020), arXiv:2006.12499 [nucl-th].
[11] G. Nijs, W. van der Schee, U. Gürsoy, and R. Snellings, Phys. Rev. Lett. **126**, 202301 (2021), arXiv:2010.15130 [nucl-th].
[12] G. Nijs, W. van der Schee, U. Gürsoy, and R. Snellings, Phys. Rev. C **103**, 054909 (2021), arXiv:2010.15134 [nucl-th].
[13] D. Everett *et al.* (JETSCAPE), Phys. Rev. C **103**, 054904 (2021), arXiv:2011.01430 [hep-ph].
[14] J. E. Parkkila, A. Onnerstad, and D. J. Kim, Phys. Rev. C **104**, 054904 (2021), arXiv:2106.05019 [hep-ph].
[15] J. E. Parkkila, A. Onnerstad, S. F. Taghavi, C. Mordasini, A. Bilandzic, M. Virta, and D. J. Kim, Phys. Lett. B **835**, 137485 (2022), arXiv:2111.08145 [hep-ph].
[16] G. Aad *et al.* (ATLAS), Phys. Rev. Lett. **116**, 172301 (2016), arXiv:1509.04776 [hep-ex].
[17] V. Khachatryan *et al.* (CMS), Phys. Rev. Lett. **116**, 172302 (2016), arXiv:1510.03068 [nucl-ex].
[18] V. Khachatryan *et al.* (CMS), Phys. Lett. B **765**, 193 (2017), arXiv:1606.06198 [nucl-ex].
[19] S. Acharya *et al.* (ALICE), Phys. Rev. Lett. **123**, 142301 (2019), arXiv:1903.01790 [nucl-ex].
[20] M. Aaboud *et al.* (ATLAS), Phys. Rev. C **97**, 024904 (2018), arXiv:1708.03559 [hep-ex].
[21] B. Abelev *et al.* (ALICE), Phys. Lett. B **719**, 29 (2013), arXiv:1212.2001 [nucl-ex].
[22] G. Aad *et al.* (ATLAS), Phys. Rev. C **90**, 044906 (2014), arXiv:1409.1792 [hep-ex].
[23] M. Aaboud *et al.* (ATLAS), Phys. Rev. C **96**, 024908 (2017), arXiv:1609.06213 [nucl-ex].
[24] V. Khachatryan *et al.* (CMS), Phys. Rev. C **96**, 014915 (2017), arXiv:1604.05347 [nucl-ex].
[25] C. Aidala *et al.* (PHENIX), Nature Phys. **15**, 214 (2019), arXiv:1805.02973 [nucl-ex].

[26] C. Aidala *et al.* (PHENIX), Phys. Rev. Lett. **120**, 062302 (2018), arXiv:1707.06108 [nucl-ex].
[27] A. Bilandzic, R. Snellings, and S. Voloshin, Phys. Rev. C **83**, 044913 (2011), arXiv:1010.0233 [nucl-ex].
[28] M. Aaboud *et al.* (ATLAS), Phys. Lett. B **789**, 444 (2019), arXiv:1807.02012 [nucl-ex].
[29] S. Chatrchyan *et al.* (CMS), Eur. Phys. J. C **73**, 2674 (2013), arXiv:1310.4554 [hep-ex].
[30] J. Adams *et al.* (STAR), Phys. Rev. Lett. **92**, 052302 (2004), arXiv:nucl-ex/0306007.
[31] B. I. Abelev *et al.* (STAR), Phys. Rev. C **75**, 054906 (2007), arXiv:nucl-ex/0701010.
[32] S. S. Adler *et al.* (PHENIX), Phys. Rev. Lett. **91**, 182301 (2003), arXiv:nucl-ex/0305013.
[33] A. Adare *et al.* (PHENIX), Phys. Rev. Lett. **98**, 162301 (2007), arXiv:nucl-ex/0608033.
[34] J. Adam *et al.* (ALICE), Phys. Rev. C **93**, 034916 (2016), arXiv:1507.06194 [nucl-ex].
[35] J. Adam *et al.* (ALICE), JHEP **09**, 164 (2016), arXiv:1606.06057 [nucl-ex].
[36] S. Acharya *et al.* (ALICE), JHEP **09**, 006 (2018), arXiv:1805.04390 [nucl-ex].
[37] S. Acharya *et al.* (ALICE), JHEP **05**, 243 (2023), arXiv:2206.04587 [nucl-ex].
[38] L. Zheng, H. Li, H. Qin, Q.-Y. Shou, and Z.-B. Yin, Eur. Phys. J. A **53**, 124 (2017), arXiv:1611.05185 [nucl-th].
[39] J. C. Dunlop, M. A. Lisa, and P. Sorensen, Phys. Rev. C **84**, 044914 (2011), arXiv:1107.3078 [hep-ph].
[40] S. Singha and M. Nasim, Phys. Rev. C **93**, 034908 (2016), arXiv:1603.01220 [nucl-ex].
[41] V. Pacík (ALICE), Nucl. Phys. A **982**, 451 (2019), arXiv:1807.04538 [nucl-ex].
[42] A. Adare *et al.* (PHENIX), Phys. Rev. C **97**, 064904 (2018), arXiv:1710.09736 [nucl-ex].
[43] B. Schenke, C. Shen, and P. Tribedy, Phys. Rev. C **102**, 044905 (2020), arXiv:2005.14682 [nucl-th].
[44] M. Strickland, Nucl. Phys. A **982**, 92 (2019), arXiv:1807.07191 [nucl-th].
[45] C. Loizides, Nucl. Phys. A **956**, 200 (2016), arXiv:1602.09138 [nucl-ex].
[46] J. L. Nagle and W. A. Zajc, Ann. Rev. Nucl. Part. Sci. **68**, 211 (2018), arXiv:1801.03477 [nucl-ex].
[47] M. Gyulassy and M. Plumer, Phys. Lett. B **243**, 432 (1990).
[48] X.-N. Wang and M. Gyulassy, Phys. Rev. Lett. **68**, 1480 (1992).
[49] J. Adam *et al.* (ALICE), Phys. Rev. C **91**, 064905 (2015), arXiv:1412.6828 [nucl-ex].
[50] V. Khachatryan *et al.* (CMS), JHEP **04**, 039 (2017), arXiv:1611.01664 [nucl-ex].
[51] J. Adam *et al.* (ALICE), (2016), 10.1140/epjc/s10052-016-4107-8, arXiv:1603.03402 [nucl-ex].
[52] J. Adam *et al.* (ALICE), Phys. Lett. B **760**, 720 (2016), arXiv:1601.03658 [nucl-ex].
[53] S. Acharya *et al.* (ALICE), Phys. Lett. B **783**, 95 (2018), arXiv:1712.05603 [nucl-ex].
[54] J. Adam *et al.* (ALICE), Phys. Rev. Lett. **119**, 102301 (2017), arXiv:1609.06643 [nucl-ex].
[55] Z.-W. Lin, C. M. Ko, B.-A. Li, B. Zhang, and S. Pal, Phys. Rev. C **72**, 064901 (2005), arXiv:nucl-th/0411110.
[56] C. Bierlich, G. Gustafson, and L. Lönnblad, Phys. Lett. B **779**, 58 (2018), arXiv:1710.09725 [hep-ph].
[57] C. Bierlich, Phys. Lett. B **795**, 194 (2019), arXiv:1901.07447 [hep-ph].
[58] T. Pierog, I. Karpenko, J. M. Katzy, E. Yatsenko, and K. Werner, Phys. Rev. C **92**, 034906 (2015), arXiv:1306.0121 [hep-ph].
[59] P. Skands, S. Carrazza, and J. Rojo, Eur. Phys. J. C **74**, 3024 (2014), arXiv:1404.5630 [hep-ph].
[60] S. H. Lim, Q. Hu, R. Belmont, K. K. Hill, J. L. Nagle, and D. V. Perepelitsa, Phys. Rev. C **100**, 024908 (2019), arXiv:1902.11290 [nucl-th].
[61] S. Acharya *et al.* (ALICE), JHEP **05**, 290 (2021), arXiv:2101.03110 [nucl-ex].
[62] J. Kim, E.-J. Kim, S. Ji, and S. Lim, J. Korean Phys. Soc. **79**, 447 (2021), arXiv:2108.09686 [nucl-th].
[63] J. D. Orjuela Koop, A. Adare, D. McGlinchey, and J. L. Nagle, Phys. Rev. C **92**, 054903 (2015), arXiv:1501.06880 [nucl-ex].
[64] K. Gallmeister, H. Niemi, C. Greiner, and D. H. Rischke, Phys. Rev. C **98**, 024912 (2018), arXiv:1804.09512 [nucl-th].
[65] A. Kurkela, U. A. Wiedemann, and B. Wu, Eur. Phys. J. C **79**, 965 (2019), arXiv:1905.05139 [hep-ph].
[66] A. Kurkela, S. F. Taghavi, U. A. Wiedemann, and B. Wu, Phys. Lett. B **811**, 135901 (2020), arXiv:2007.06851 [hep-ph].
[67] V. E. Ambrus, S. Schlichting, and C. Werthmann, Phys. Rev. D **105**, 014031 (2022), arXiv:2109.03290 [hep-ph].
[68] K. Werner, B. Guiot, I. Karpenko, and T. Pierog, Phys. Rev. C **89**, 064903 (2014), arXiv:1312.1233 [nucl-th].
[69] S. Acharya *et al.* (ALICE), Eur. Phys. J. C **81**, 630 (2021), arXiv:2009.09434 [nucl-ex].
[70] K. Aamodt *et al.* (ALICE), JINST **3**, S08002 (2008).
[71] E. Abbas *et al.* (ALICE), JINST **8**, P10016 (2013), arXiv:1306.3130 [nucl-ex].
[72] G. Aad *et al.* (ATLAS), Phys. Rev. Lett. **110**, 182302 (2013), arXiv:1212.5198 [hep-ex].
[73] See Supplemental Material at `http://link.aps.org/supplemental/10.1103/PhysRevC.xx.xxxxxx` for LMTF method and two- particle correlation functions used in the paper in further detail with additional results from AMPT model calculations and it includes Refs. [74,75].
[74] N. Mallick, S. Prasad, A. N. Mishra, R. Sahoo, and G. G. Barnaföldi, Phys. Rev. D **107**, 094001 (2023), arXiv:2301.10426 [hep-ph].
[75] J. Adams *et al.* (STAR), Phys. Rev. C **72**, 014904 (2005), arXiv:nucl-ex/0409033.

Appendix: Supplemental Material

In this section, the low multiplicity template fits and two-particle correlation functions of the models used in the paper are described in further detail. Also, a few additional figures are provided for the η gap and multiplicity dependence flow results that are from the AMPT String Melting model calculations.

1. Low multiplicity template fit

Fig. 12 shows the LM-template fit results for pp $\sqrt{s} =$ 13 TeV TPC-FMDA correlations for three models in the 0–20% multiplicity percentiles. In all columns, the per-trigger particle yield is shown as a function of $\Delta\varphi$. The black markers represent HM events, the blue bands represent fit, and the red squares represent LM events. Orange and green bands represent the extracted harmonic flow components. The bottom panels show a zoomed-in view of the near-side region to better visualize the data.

The analysis done with the EPOS4 model calculations results to relatively flat near-side LM yields, while both PYTHIA8 models show distinct near-side ridges. Notably, PYTHIA8 Shoving results as the largest near-side yields in the LM events, which are comparable to the yields in the HM events. Additionally, in Fig. 12, the PYTHIA8 models have positive v_3 and negative v_2, while the EPOS4 model has positive v_3 and v_2.

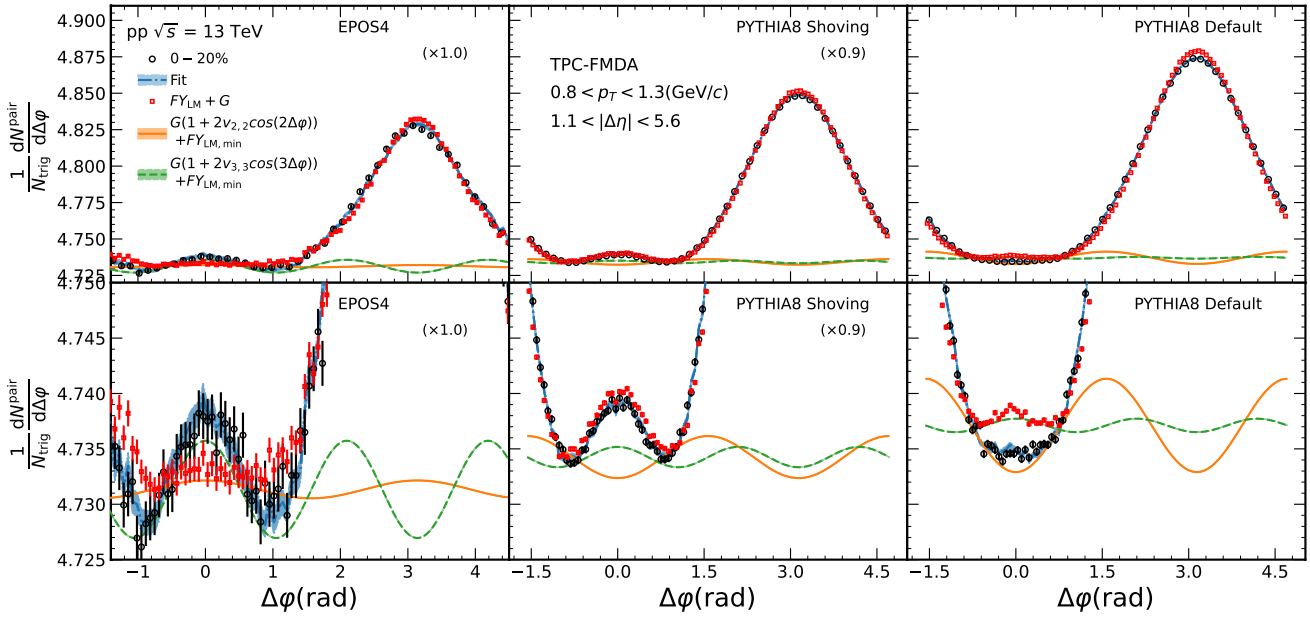

FIG. 12. The template fit results with the LM-templates from EPOS4, PYTHIA8 Shoving and PYTHIA8 Default models. The black markers shows the signal for the 0–20% multiplicity percentile together with its fit shown as a blue band. The red squares correspond to the scaled LM signal. The orange and green curves correspond to the extracted v_2 and v_3 signals, respectively.

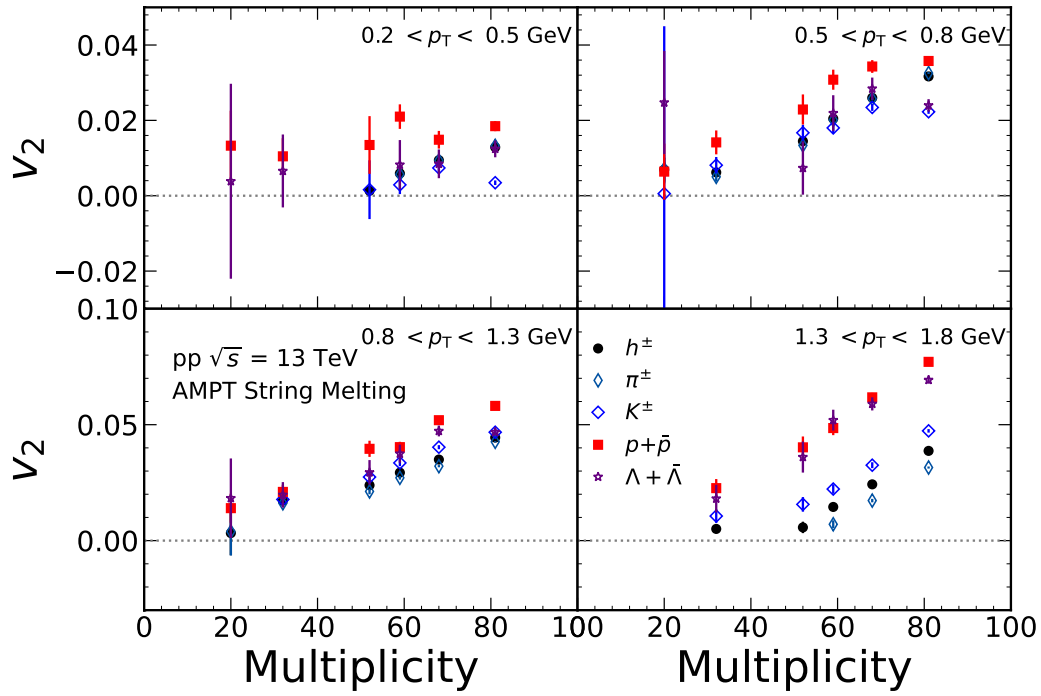

FIG. 13. The multiplicity dependence of v_2 with various p_T bins for different particle species in pp collisions at $\sqrt{s} = 13$ TeV from the AMPT String Melting model calculations.

2. Multiplicity and η gap dependence

In Fig. 13, we present the magnitude of v_2 as a function of multiplicity for various particle species in four p_T ranges as an addition to Sec. IV, where only two high p_T ranges were provided. The conclusions are same for $0.5 < p_T < 0.8$GeV/c as they were for $0.8 < p_T < 1.3$GeV/c and $1.3 < p_T < 1.8$GeV/c. In the case of the lowest p_T range shown in the top left panel of Fig. 13, we observe that the multiplicity dependence is weaker than with other p_T ranges. Furthermore, the ordering in the v_2 magnitudes between different particle species is visible, as discussed in the previous section. At higher p_T ranges, the magnitudes of v_2 are clearly separated between mesons and baryons in higher multiplicities.

The panel for the AMPT String melting model in Fig.8 is zoomed in Fig. 14 and the ratio of the results from the different η gap to the default selection is shown in the bottom panel. In the low p_T regions, v_2 are increased by 50% and in high p_T regions, a factor of two respectively.

3. The number of constituent-quark scaling in large-system collisions at the RHIC and LHC energies

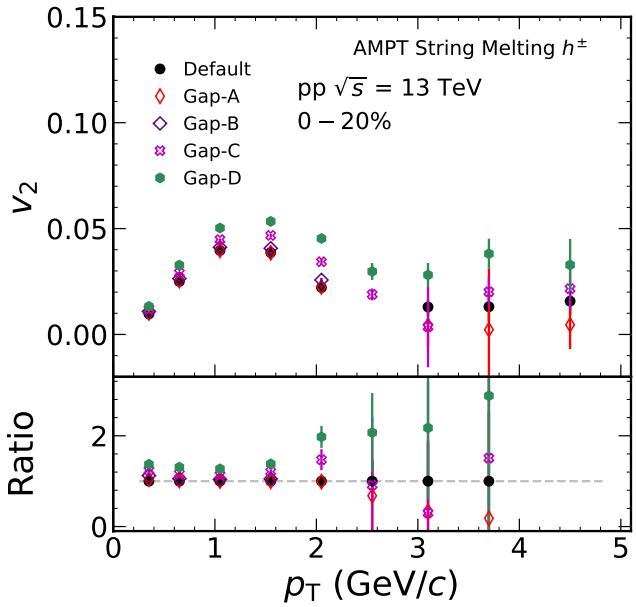

FIG. 14. The p_{T}-differential v_2 for different η gap interval in pp collisions at $\sqrt{s}$ = 13 TeV for AMPT String Melting calculations are shown for the charged particles.

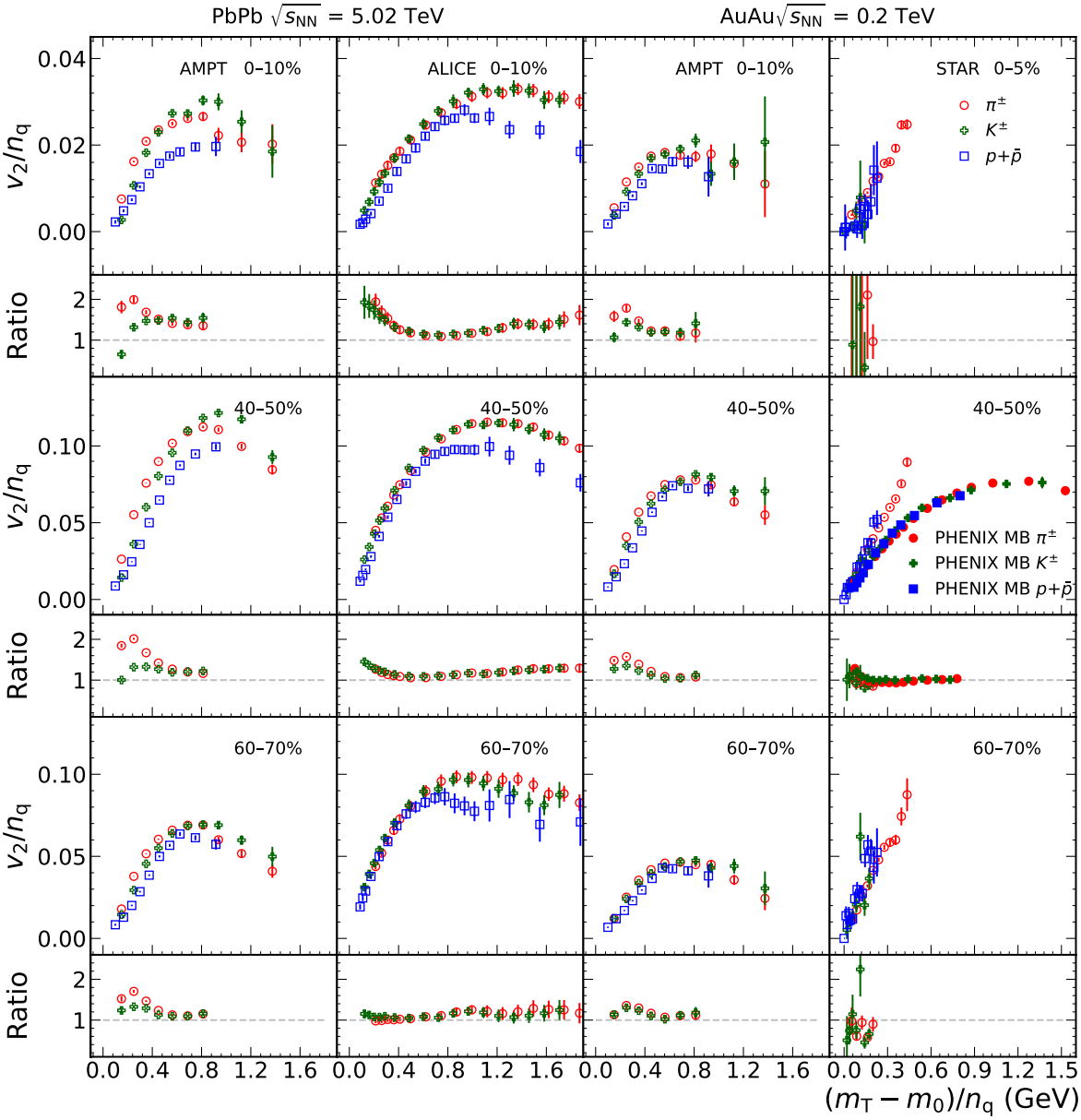

FIG. 15. Centrality dependence of constituent quark scaling of v_2 as a function of $(m_T - m_0)/n_q$ for different particle species from the RHIC [33, 75] and LHC energies [36]. They are compared to the AMPT calculations [74]. The results from the PHENIX collaboration at RHIC are shown only for the minimum bias Au-Au collisions [33].

Figure 15 shows the dependence of v_2 on transverse kinetic energy, normalized by the number of quark constituents (n_q), in experimental data and AMPT calculations [74] for PbPb and AuAu collisions at $\sqrt{s_{NN}} = 5.02$ TeV (LHC) [36] and 0.2 TeV (RHIC) [33, 75] energies, respectively. The first two columns are for PbPb collisions at LHC energy and the last two columns are for AuAu collisions at RHIC energy in three centrality ranges. The bottom panel of each centrality interval shows the ratio to proton results. The scaling of the number of constituent quarks (NCQ) is found to be different between the data and AMPT at LHC energy. Specifically, the proton is more deviated from other species in AMPT compared to the data. Furthermore, the centrality dependence of the scaling is weak, and the ratios to proton results decrease as the centrality increases. These findings suggest that NCQ scaling is dependent on the energy and centrality of the collisions. At RHIC energy, a similar trend was observed for AMPT, but the data showed good scaling behavior for all centrality classes. As seen in Fig. 10,

this ordering in pp collisions from the AMPT calculations was quite distinct from that seen in large-system collisions. In particular, the ratios to the protons results is less than 1 for low p_{T} ranges in pp collisions while they are larger than 1 except for few data points in the large-system collisions.

4. Two dimentional correlation functions

Fig. 16 and Fig. 17 show two-particle correlation functions from PYTHIA8 Shoving and EPOS4 in two different multiplicity percentiles (0–20% and 60–100%). The figures are divided into six panels, each panel showing correlation functions from separate detector combinations. The $\Delta\eta$ gaps used in our analysis are expressed as colored lines parallel to $\Delta\varphi$ line marking the minimum value of each gap. In the lower $\Delta\eta$ region, TPC-FMDA and TPC-FMDC results are showing clear peaks. For TPC-FMDA and FMDA-FMDC, a noticeable decrease in the amount of correlations can be seen when going into larger $\Delta\eta$ regions relative to TPC-FMDC. This is also seen in the other models as well (see Fig. 3 and Fig. 4). The correlations from FMDA-FMDC results are showing larger without a clear peak. For TPC-FMDC, the away-side yields are elongated along the whole $|\Delta\eta|$ range.

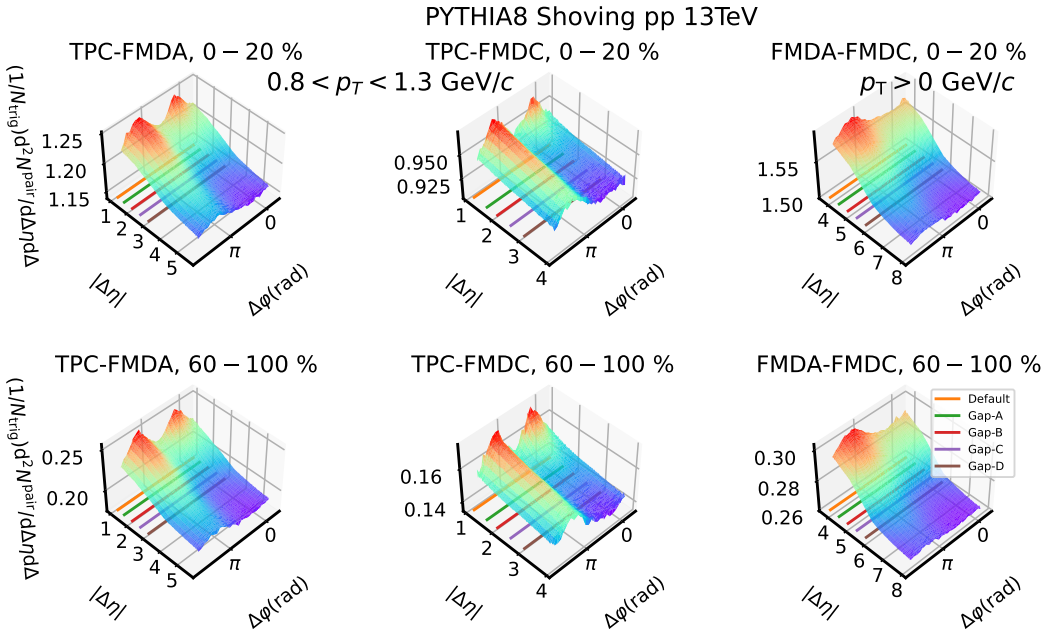

FIG. 16. Two-particle correlation functions as functions of $\Delta\eta$ and $\Delta\varphi$ for HM (0–20%, top panels) and LM (60–100%, bottom panels) events by using various combinations of the detectors in $\sqrt{s} = 13$ pp collisions from PYTHIA8 String Shoving calculations. The intervals of $p_{\mathrm{T,\,trig}}$ and $p_{\mathrm{T,\,assoc}}$ are $0.8 < p_{\mathrm{T}} < 1.3$ GeV/c with TPC and $p_{\mathrm{T}} > 0$ GeV/c with FMDA or FMDC.

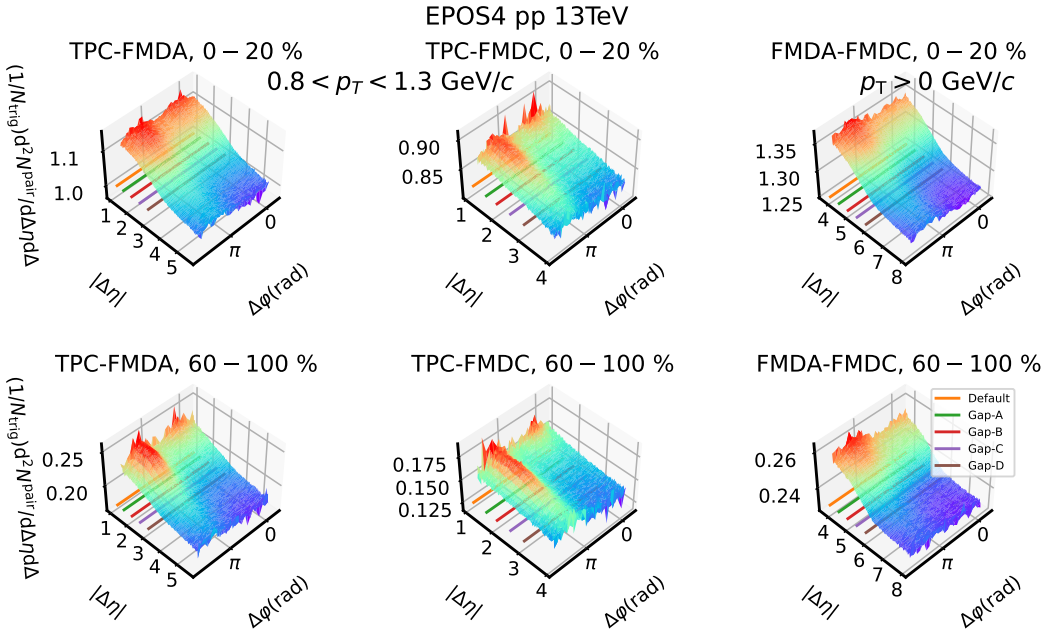

FIG. 17. Two-particle correlation functions as functions of $\Delta\eta$ and $\Delta\varphi$ for HM(0–20%, top panels) and LM(60–100%, bottom panels) events by using various combinations of the detectors in $\sqrt{s} = 13$ pp collisions from EPOS4 calculations. The intervals of $p_{\mathrm{T,\,trig}}$ and $p_{\mathrm{T,\,assoc}}$ are $0.8 < p_{\mathrm{T}} < 1.3$ GeV/c with TPC and $p_{\mathrm{T}} > 0$ GeV/c with FMDA or FMDC.